Continuous online-monitoring of Ice Nucleating Particles: development of the automated Horizontal Ice Nucleation Chamber (HINC-Auto)

Cyril Brunner[1] and Zamin A. Kanji[1]

[1]Institute for Atmospheric and Climate Science, ETH, Zurich, 8092, Switzerland

Correspondence: C. Brunner (cyril.brunner@env.ethz.ch) and Z.A. Kanji (zamin.kanji@env.ethz.ch)

Abstract. The incomplete understanding of aerosol-cloud interactions introduces large uncertainties when simulating the cloud radiative forcing in climate models. The physical and optical properties of a cloud, as well as the evolution of precipitation, are strong functions of the cloud hydrometeor phase. Aerosol particles support the phase transition of water in the atmosphere from a meta-stable to a thermodynamically preferred, stable phase. In the troposphere, the transition of liquid droplets to ice crystals

5 in clouds, via ice nucleating particles (INPs) which make up only a tiny fraction of all tropospheric aerosol, is of particular relevance. For accurate cloud modeling in climate projections, the parameterization of cloud processes and information such as the concentrations of atmospheric INPs are needed. Presently, no continuous real-time INP counter is available and the data acquisition still requires a human operator. To address this restriction, we developed HINC-Auto, a fully automated online INP counter, by adapting an existing custom-built instrument, the Horizontal Ice Nucleation Chamber. HINC-Auto

10 was able to autonomously sample INPs in the immersion mode at a temperature of 243 K and a water saturation ratio of 1.04 for 97% of the time for 90 consecutive days. Here we present the technical setup used to acquire automation, discuss improvements to the the experimental precision and sampling time, and validate the instrument performance. In the future, the chamber will allow a detailed temporal analysis (including seasonal and annual variability) of ambient INP concentrations observing repeated meteorological phenomena compared to previous episodic events detected during campaigns. In addition,

15 by deploying multiple chambers at different locations, a spatio-temporal variability of INPs at any sampling site used for monitoring INP analysis can be achieved for temperatures ≤ 243 K.

1 Introduction

The interaction between aerosols and clouds contributes to the global energy budget by directly influencing the radiative forcing of the climate system. Yet, predictive climate models struggle to accurately simulate aerosol-cloud interactions, e.g. the

20 Intergovernmental Panel on Climate Change attributed a low confidence level of the aerosol-cloud interactions in their fifth assessment report (Boucher et al., 2013). Clouds containing ice have special relevance to the Earth's climate. Not only does the cloud phase strongly influence climate-relevant physical properties, such as albedo (e.g., Sun and Shine, 1994; Lohmann and Feichter, 2005), but ice is also shown to be responsible for the development of most mid-latitude precipitation processes (e.g., Mülmenstädt et al., 2015). Consequently, it is essential to understand the mechanism of ice formation within mixed-phase

25   clouds. One such mechanism is immersion freezing, the formation of ice crystals on ice nucleating particles (INPs) immersed in liquid droplets (Vali et al., 2015), which has been studied extensively in laboratory studies (see e.g., Zuberi et al., 2002; DeMott et al., 2003; Marcolli et al., 2007; Lüönd et al., 2010; Niemand et al., 2012; Murray et al., 2012; Atkinson et al., 2013; Hiranuma et al., 2015). A large number of field studies based on intensive observation periods to quantify the concentration, properties, identity and sources of immersion mode INPs have also been reported (see e.g. Dufour, 1862; Rogers and Vali,

30   1978; Demott et al., 2003; Richardson et al., 2007; Chou et al., 2011; Boose et al., 2016; Lacher et al., 2017). These studies have substantially improved our understanding of such atmospheric INP properties and sources, but some aspects such as diurnal variability, seasonal and and annual trends as well as general spatio-temporal variability of INPs remains poorly constrained (see e.g., Demott et al., 2011; Cziczo et al., 2017; Kanji et al., 2017; Lacher et al., 2018) and insufficiently understood, needing more research to accurately represent atmospheric ice formation in climate models (Demott et al., 2010; Phillips et al., 2013).

35   For example most field studies on INP measurements in the atmosphere have to focus on cases rather than drawing conclusions about the long term trends because of the lack of such data sets. To quantify the free troposphere INP concentration in the Swiss Alps, data from 9 field campaigns over the course of 3 years was required in order to quantify this parameter representing a background INP concentration at a single temperature (242 K) (Lacher et al., 2018), making such research data costly and inaccessible to cloud modellers. Furthermore, with the lack of long term frequent data sets, cloud model research is limited

40   to the small specific case studies for validating INP parameterizations in global or regional climate models (see e.g., Niemand et al., 2012).

To sample INPs, either offline or online techniques are available. In offline INP counters, air is sampled through a filter or an aerosol-to-liquid cyclone impinger. The filter is washed in pure water to extract the sampled aerosols while the cyclone is filled

45   with a small amount of water in which the aerosols accumulate. The sample is then divided into small droplets on cold stages. The freezing of the droplets as a function of temperature allows deducing the INP concentration of the sampled air (Vali, 1971). The advantages of the offline technique are the ability to detect low INP concentrations thus reporting INP concentrations at fairly low (272 K) as well as high supercooling (235 K) (e.g., Conen et al., 2015; Petters and Wright, 2015; Mignani et al., 2019; Wex et al., 2019; Brubaker et al., 2020). Furthermore, the ability of having the aerosols contained for future additional

50   analysis is also possible because not all the sample has to be used in this method of processing and neither is the analysis method of the sample destructive. This comes at the sacrifice of lower time resolution due to the continuous sampling for 8 - 12 hours or more per sample, in order to generate appropriate signal to noise ratio in the freezing spectra. Additional drawbacks include the chance for sample modification when INPs impact the filter or during sample handling and storage (e.g., Cziczo et al., 2017, and references therein). Most recently, Beall et al. (2020) found losses of up to 72% to INP concentration caused

55   by storage at room temperature versus losses of 25% by storage at 253 K over up to 166 days.

Online techniques sample and detect INPs in one step in real time. The measurement of INPs in ambient air is challenging since their number concentrations are on the order of 10^{-1} to 10^2 std L^{-1} (at 242 K, S_w = 1.04, (see e.g., Lacher et al., 2018; Kanji et al., 2017)) while the sensitivity of portable INP counters is on the order of 10^{-2} std L^{-1} (Cziczo et al., 2017). This

60 makes online counters good candidates for reporting INP concentrations at moderate (with the presence of aerosol concentrators) to high supercooling ($\leq$ 248 K). Online counters have the advantage of resampling INPs downstream of cloud chambers for further single particle analysis, but often times these measurements are technically challenging and time consuming because of the low concentrations of INPs. Online and offline data acquisition of INP concentrations needs human operation and is subsequently limited to isolated or planned field campaigns. A handful of ambient INP measurements do exist (Kanji et al.,

65 2017, and references therein). A prime limitation for the absence of long term monitoring data sets is that online real-time measurements of INP concentrations via INP counters requires human operators. Presently, no automated online INP counter is available (Cziczo et al., 2017; Lacher et al., 2017). Offline techniques can be automated in their sampling but require substantial sample handling, storage, and finally processing of samples to derive INP concentrations, all by dedicated trained scientists. Furthermore automated aerosol sampling techniques will suffer significantly lower time resolution with the advantage of quan-

70 tifying INP concentrations at higher temperatures compared to online techniques (Cziczo et al., 2017, and discussion therein).

In this work we present an automated continuous online INP counter, HINC-Auto. Besides a technical description and findings to enhance the chamber precision and sampling time, the chamber is validated with laboratory tests and experiments are compared to a theoretical model. HINC-Auto has been implemented for continuous monitoring of INPs at center temperature

75 (T) = 243 K and and saturation with respect to water (S_w) = 1.04 at the High Altitude Research Station Jungfraujoch (JFJ, 3580 m a.s.l., 46°33' N, 7°59' E). From the collected data set, since Feb 2020, it is expected that a continuous and more detailed temporal analysis of ambient INP concentrations will be possible, thereby observing repeated meteorological episodes compared to previous singular events detected during a single field campaign.

2 Materials and Methods

80 ### 2.1 Working principle

In the 1980s, continuous flow thermal gradient diffusion chambers were developed to study cloud condensation and ice nucleation (Hussain and Saunders, 1984; Al-Naimi and Saunders, 1985; Tomlinson and Fukuta, 1985; Rogers, 1988). Continuous flow chambers (CFC) used a temperature gradient ∇T to produce water vapor supersaturation in the region between two water- or ice-covered walls. Rogers (1988) defined the term continuous flow thermal gradient diffusion chamber (CFDC) and

85 described the underlying working principle: The annular volume between two vertically oriented concentric cylinders forms the chamber's cavity. The outer and inner walls of the chamber are chilled individually and are covered with a thin layer of ice. For the experiment, one wall is held at a warmer temperature than the other wall, thereby, heat as well as water vapor are diffused from the warm to the cold wall, forming radially linear steady-state temperature and water vapor pressure fields. Because the saturation vapor pressure with respect to water and ice are exponential functions, a supersaturation with respect to

90 ice, $S_\mathrm{i} > 1$, is formed between the two walls. Supersaturation with respect to water $S_\mathrm{w} \geq 1$ can be achieved with large enough temperature gradients. A steady flow passes coaxially through the chamber, entraining the sample aerosols in its center lamina. The surrounding sheath air is filtered before entering the chamber. T and S are adjusted to the desired experimental conditions.

A more detailed description can be found in Rogers (1988).

95   The CFDC of Kumar et al. (2003) was developed to probe aerosols and investigate their ability to acts as cloud condensation nuclei (CCN). In contrast to the design of Rogers, the chamber consisted of two horizontally oriented parallel walls. Kanji and Abbatt (2009) altered the design to the University of Toronto CFDC (UT-CFDC) to study ice nucleation at low temperatures. A horizontally oriented ice nucleation chamber offers two major advantages: first, the buoyancy of the air within the chamber resulting from the temperature gradient stabilizes the desired laminar flow. In vertically oriented chambers, the flow is oriented

100   from the top to the bottom. The buoyancy at the warm wall favours an upward vertical air movement which counteracts the overall flow direction. Likewise, the reduced buoyancy at the cold wall adds a relative sinking motion in the proximity of the cold wall. If the temperature gradient is increased such that the shear between the lamina overcomes the fluid's viscous forces, the flow becomes turbulent. The increased mixing not only dislocates the sample particles away from their desired center lamina but also equalizes the temperature and water vapor profiles. The set conditions then may deviate from the assumed values

105   (Rogers, 1988; Stetzer et al., 2008). This happens at gradients larger than 10-15 K, depending on the center lamina temperature (Garimella et al., 2016). Secondly, in horizontally oriented chambers the vapour diffused to the cold wall forming frost tends to stay on the bottom wall because of gravity. In a vertical ice nucleation chamber, the ice grown on the cold wall has the tendency to break off, get carried along with the downward moving sheath flow and is in danger of being misinterpreted as ice formed on an INP. The biggest drawback of the horizontal orientation is the sedimentation of hydrometeors or large aerosol particles.

110   The hydrometeors have to grow to a size of $d \geq 1\,\mu m$ to be detected by the sensor placed at the outlet. For particles $\geq 5\,\mu m$, the terminal sedimentation velocity is such that the hydrometeors are subject to gravitational settling and, depending on their residence time (τ), will not be sampled by the detector.

Lacher et al. (2017) presented the Horizontal Ice Nucleation Chamber (HINC), a close adaption of the UT-CFDC. HINC's

115   record sampling times of 14 h make the chamber's design best suited to be adopted for continuous measurement of ambient INPs. A basic illustration of HINC is shown in Figure 1.
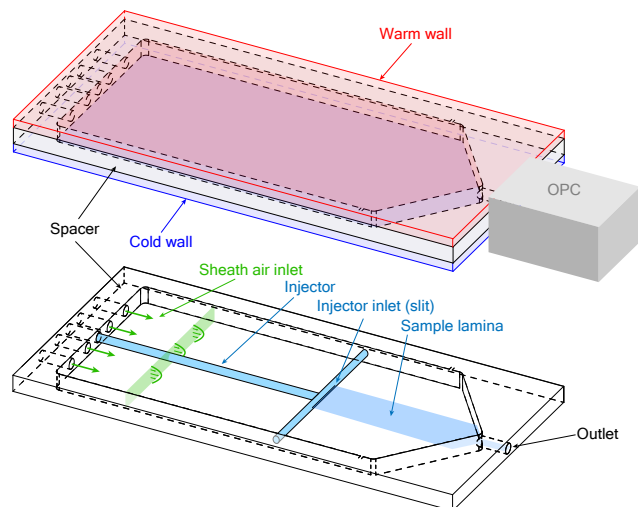
Figure 1. A schematic of HINC, the building platform of HINC-Auto. Top: the entire chamber, bottom: the internal parts.

2.2 HINC-Auto technical setup
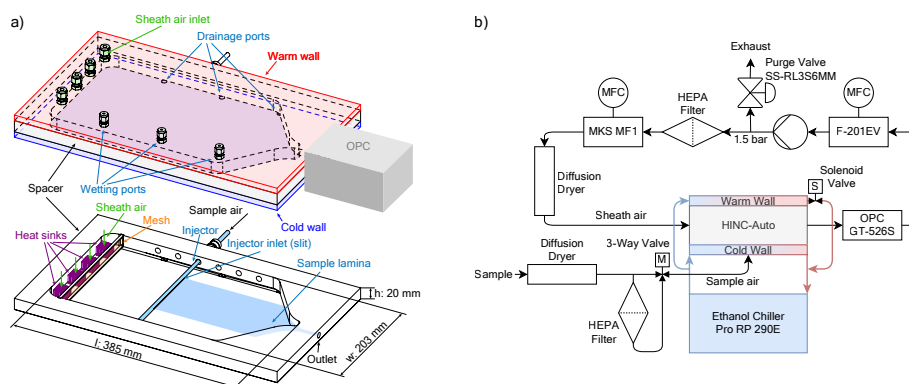
Figure 2. A schematic of HINC-Auto. a) Top: the entire chamber, bottom: the internal parts. b) External components and flow setup.

Figure 2a shows a schematic of HINC-Auto and 2b the external components and flow setup. The chamber consists of two aluminum cooling walls, with a 25 µm copper plating to avoid growth of mold. The chamber walls are cooled with an external

120 recirculating ethanol chiller (Lauda PRO RP 290E), operated in a parallel-flow constellation to the air flow within the chamber. A polyvinylidene fluoride (PVDF) spacer separates the two chamber walls. A cut-out section within the PVDF spacer and the inner surfaces of the metal walls forms the cavity of the chamber. The inner metal walls are covered with self-adhering borosilicate glass microfibre filter paper (PALL 66217, 1 µm, 8x10") which is wetted with water and acts as reservoir for water vapor in order to create ice and/or water (super)saturation. During normal operation, the temperature of the bottom wall is equal to or

125 lower than the one of the top wall. The chillers PID-controller directly controls the bottom wall temperature. A Y-connection

just upstream of the bottom wall cooling inlet allows some of the chilled ethanol flow to diverge and flow through the top wall. At the top wall cooling exit, a solenoid valve controls the flow rate of the ethanol through the top wall before feeding it back into the re-circulating bath via the ethanol outlet of the bottom (colder) wall. If the top (warmer) wall is too warm the solenoid is actuated by a PI-controller and if the top wall is too cold, a 12V fan blows room air at the outer surface of the warm wall

130   to increase its temperature. Three thermocouples (Transmetra TEMI313, type K, NiCr-Ni) monitor the temperature on each wall. To expose the aerosol particles within the sample air to a predefined temperature and supersaturation, the sample air has to remain in the center plane between the two chamber walls. Therefore, the center lamina is sandwiched between equal parts of particle-free sheath air. The sheath to sample air ratio is 9 to 1. The mass flow controlled (mass flow controller (MFC) MKS MF1, full scale range: 5 std L min^{-1}, set to 2.547 std L min^{-1}) and dried (diffusion dryer, $S_w \leq 0.008$ at 20 °C, filled with

135   4 Å-molecular sieve) sheath air enters the chamber through four holes in the top wall and is blown on to copper heat sinks mounted on the bottom wall. The sheath air is thereby rapidly chilled and flows through a mesh which equilibrates the flow and decreases the degree of turbulence. The weaving plain type 304-stainless steel wire mesh has a mesh-size of 250 mesh inch^{-1} and a wire diameter of 0.04 mm. It spans over the entire width and height of the chamber's cavity (See Fig. 2a). The filter paper coats the cooling walls only downstream of the mesh. A horizontally aligned injector with a outer diameter of 6.35

140   mm and a slit of 0.4x100 mm^2 is used to guide the sample air into the chamber. The sampled air also passes a diffusion dryer identical to the sheath flow dryer before entering the injector. The injector is mounted through one of six holders in the side wall of the spacer. All unused holes are plugged. Placing the injector in a hole further upstream allows to increase the particle residence time and vice versa. A 6-channel optical particle counter (OPC, MetOne GT-526S) detects the number and size of the particles exiting the chamber via the outlet. A MFC downstream of the OPC (Bronkhorst, F-201EV, full scale range: 3.5

145   std L min^{-1}) is set to 2.83 std L min^{-1} (defined by the specifications of the OPC). The sample air flow rate of 0.283 std L min^{-1} results from the difference of the volume flow exiting the chamber through the OPC and the sheath air directed into the chamber. Consequently, a well sealed chamber is crucial for a representative operation. Downstream of the OPC and the MFC, a vacuum pump (KNF, N 035 ATE) is used to generate sufficient pressure drop over the MFC and to increase the pressure after the pump. A purge valve (Swagelok, SS-RL3S6MM) purges excess air above the set absolute pressure of 1.5 bar. The air is

150   filtered with a HEPA filter and recycled back into the sheath air MFC.

     During operation, water vapor diffuses from the top to the bottom wall, depleting the top wall of the ice layer while adding additional ice to the bottom wall. To maintain the desired supersaturation within the chamber, the top wall ice layer needs to get replenished by re-wetting the filter paper at temperatures $T > 273$ K. This rewetting procedure requires tilting the chamber

155   by 25° using a linear motor to allow excess water and water collected on the cold wall to drain. A peristaltic pump with a flow rate of 10 ml min^{-1} pumps 40 ml water from a water reservoir into one of the three wetting ports, located on the top cooling plate. Two solenoid valves alternate the used wetting port every 10 seconds. During the rewetting procedure a second peristaltic pump with a flow rate of 65 ml min^{-1} is used to drain excess water which is recycled back into the rewetting reservoir. The reservoir is initially filled with 500 ml double-deionized water. The reservoir is protected from day light while a piece of copper

160   and a UV-LED protects the water from spoilage. The total water uptake of the chamber is 100 ml month^{-1}. The molecular

sieves in the diffusion dryers need to be replaced every 30-60 days, depending on the ambient relative humidity. Sensors are used to check both sheath and sample air relative humidity to determine when the molecular sieves require replenishing.

2.3 Design changes

HINC showed differences between the measured and the calculated particle residence times as shown in Figure 3a. The par-

165 ticle residence times were measured with pulse experiments, where a brief pulse of particles is injected into HINC and then compared to the delayed temporal evolution of the particle counts exiting the chamber. To analyze the discrepancy, a 3D computational fluid dynamics (CFD) simulation was carried out (STAR-CCM+ V13.04.010). The CFD simulation was validated with a particle image velocimetry (PIV) experiment. A detailed description of CFD simulation and the PIV experiment can be found in the appendix (A1). Only after modelling the tubing of the sheath air and corresponding union tee and union cross to

170 distribute the sheath air outside of the chamber, the CFD simulation and the PIV-experiment came into good agreement. The validated simulation showed persistent high velocity regions downstream of the sheath air inlets (see Figure A2) which are not in agreement with the anticipated flow velocities. This explains the lower residence time in pulse tests compared to the calculated residence time, which assumed ideal velocity distributions within HINC. Besides the high velocity jet regions (Figure A2), reversed flows are also present within the chamber, forming two large counter rotating vortices. Particle sedimentation

175 experiments with HINC also confirmed the two vortices. To smooth the flow field within the chamber and achieve a more consistent desired unidirectional flow field, a mesh was introduced 20 mm downstream of the sheath air injector holes. PIV experiments with the mesh installed in HINC showed the anticipated homogenization of the flow velocity. With HINC-Auto pulse tests are now in good agreement with the calculated values as seen in Figure 3b. Therefore, no additional PIV experiments and CFD simulations were performed with HINC-Auto.
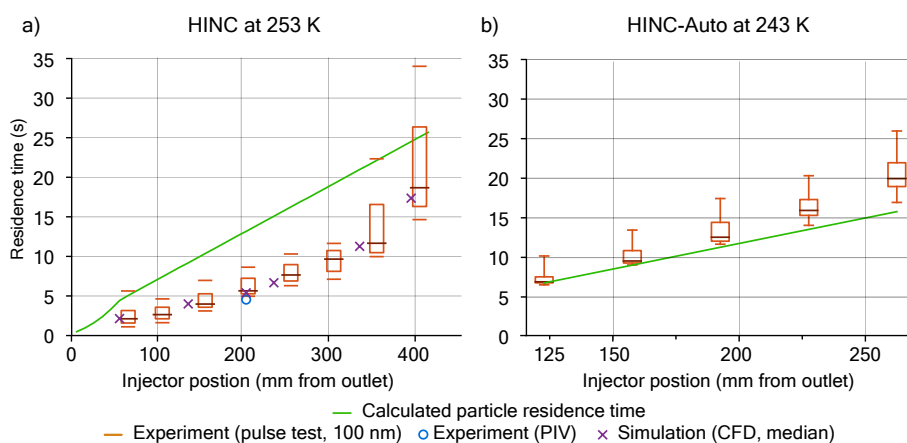
Figure 3. Calculated and measured particle residence time in a) HINC for different injector positions at $T = 253$ K and b) HINC-Auto at T = 243 K. Box plots from pulse experiments: median with 25/75% quartiles, whiskers: 5/95% quantiles. Median of PIV experiment (circles, $T = 288$ K) and CFD simulation (crosses, $T = 243$ K).

2.3.1 Reduction of rewetting duration

Maximizing the time HINC-Auto is sampling ambient air for INPs requires the duration of the rewetting procedure to be minimal. The limiting factor is warming up and cooling down the chamber from the working temperature (i.e. 243 K) to temperatures above the melting point of water (e.g. 293 K) and vice versa. The time to warm up and cool down the chamber is mostly set by the chiller's performance and by the heat capacity of the chamber itself. The new chiller (Lauda PRO RP 290E) had the best performance in comparison to the available products and their parameters, such as cooling power between 290 and 240 K, size, weight and price. Furthermore we decided to minimize the chamber's total heat capacity by machining the walls in aluminum instead of copper. A heat conduction analysis using the Finite Element Method in STAR-CCM+ V13.04.010 revealed sufficient temperature equality ≤ 0.02 K at $T = 243$ K across both walls when changing from copper to aluminum, despite the 70% lower thermal conductivity. The 3D CDF simulation revealed for the supersaturation to need a substantial part of the chamber length to equilibrium to the set conditions. For $T = 243$ K and $S_\mathrm{w} = 1.04$ a 96% equilibration ($S_\mathrm{w} = 1.00$) was reached just 20 cm of the sheath air inlets (43% of the entire chamber length in HINC). A faster equilibration allows for a reduction of the chamber length, and subsequently, a further reduction in total heat capacity. To be more time efficient in studying the impact of the chamber length, a numerical 2D diffusion model approach was chosen over 3D CFD simulation. The newly developed 2D diffusion model has been validated with the analytical solution by Rogers (1988) and the 3D CFD simulation. In order for the supersaturation to equilibrate to the set supersaturation, the temperature as well as the water vapor distribution along the chamber's height have to equilibrate from the initial conditions. Figure 4a shows the equilibration of the supersaturation profile in HINC to be temperature limited when injecting sheath air at $T_{sheath\ air} = 298$ K with a dew point of $T_d = 233$ K while the chamber is set to $T = 243$ K and $S_\mathrm{w} = 1.04$. By precooling the sheath air to $T_{sheath\ air} = 248$ K the chamber can be shortened by 10 cm to facilitate an identical degree of supersaturation equilibration during the final 10 seconds (see Figure 4b). Larger residence times than 10 seconds are prone to hydrometeor sedimentation and are therefore not targeted. Precooling is achieved by blowing the sheath air onto heat sinks, mounted on the cold wall just upstream of the mesh. The mentioned changes and the new chiller decrease the duration of rewetting from 110 min with HINC to 50 min with HINC-Auto.
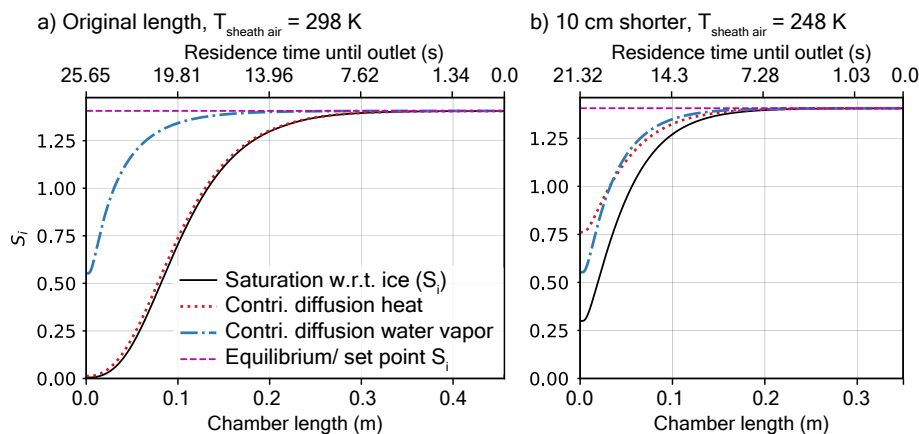
Figure 4. Simulated ice supersaturation development along the chamber's center lamina and contributing factors diffusion of heat and water vapor for a) original chamber length of 45.7 cm and sheath air injected at ambient temperature ($T_{sheath\ air}$ = 298 K) and b) with 10 cm reduced chamber length and precooled sheath air to $T_{sheath\ air}$ = 248 K.

2.3.2 Change of the axis of rotation during the rewetting procedure
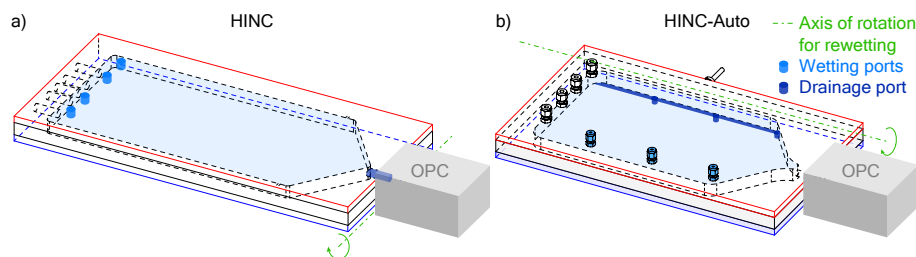
Figure 5. Illustration of the axis of rotation, location of wetting and drainage ports on a) HINC and b) HINC-Auto.

205 When rewetting HINC, the optical particle counter (OPC) has to be disconnected from the chamber's outlet to allow excess water to drain. HINC is thereby tilted 23° around an axis parallel to the width of the chamber (see Figure 5a). During rewetting HINC-Auto is tilted 25° around an axis parallel to the length of the chamber. This allows for the OPC to stay attached but required 3 additional drainage ports in the bottom wall, located just below the spacer's side wall(see Figure 5b).

2.3.3 Software

210 The chamber is controlled via a newly developed guided user interface programmed using Python 3.7 and corresponding open source packages. The postprocessing of INP concentrations is done in real time. HINC-Auto can be accessed and controlled remotely if a internet connection is available on site.

2.4 Derivation of the INP concentration

Immersion mode INP measurements are performed by sampling at T = 243 K and S_w = 1.04. At these conditions, CCN should
215   activate to supercooled droplets, and INPs, which are active at 243 K, form ice crystals. The size of the hydrometeors exiting
the chamber is used to differentiate between liquid droplets and ice crystals because ice grows to larger sizes at the prevailing
conditions ($S_i \gg S_w$). Differential measurements between the total aerosol inlet and immediately downstream of the chamber
with an OPC were used to determine particle losses. The transmission fraction of ambient particles $\geq$ 2 μm through the tubing
and the warm, dry chamber on the JFJ is 33%. No ambient particles $\geq$ 3 μm were transmitted.

220

Diffusional growth calculations at the described T and S_w conditions predict a maximum droplet size of d = 4.99 μm
(Zurich, 965 hPa, τ = 9.1 s) and d = 4.24 μm (JFJ, 645 hPa, τ = 6.1 s) for large particles with an initial diameter of d_0 = 2
μm. However, when accounting for the supersaturation equilibration within the chamber using the 2D-Diffusion model, the
calculated diffusional growth along the particle's trajectories should result in hydrometeors of smaller sizes. For an identical
225   initial radius, liquid droplets are calculated to grow to a maximum size of d = 3.31 μm (Zurich, 965 hPa, τ = 9.1 s) and d =
2.36 μm (JFJ, 645 hPa, τ = 6.1 s). Measurements of a highly hygroscopic aerosol, ammonium nitrate with an initial mobility
diameter of d_m = 200 nm (for the sample preparation see Section results/validation) show the onset of cloud droplets (no ice
crystals since T > 235 K) in the 3 μm-size bin at S_w = 1.038, as seen in Figure 6a, and support the calculated maximum size
of 3.31 μm at S_w = 1.04. The impact on the final diameter for an initial size of $d_{0_{0.2}}$ = 200 nm compared to $d_{0_{2.0}}$ = 2 μm is
230   -0.414 μm ($d_{2.0}$ = 4.99 vs. $d_{0.2}$ = 4.57 μm at 965 hPa and τ = 9.1 s). Therefore, for experiments performed at T = 243 K and
S_w = 1.04, all particles detected in the size bin $\geq$ 4 μm are considered to be ice crystals formed on INPs. Figure 6b shows a
measured activated fraction (AF) curve of ambient air on the JFJ during a high INP concentration period (7:05 22. March 2020,
UTC). AF is the ratio of all particles, that are detected in the indicated size bin, to all sampled particles, measured with a CPC
within the sample flow. The onset of cloud droplets in the $\geq$ 0.3 μm size bin exactly at S_w = 1 demonstrates the accuracy of
235   HINC-Auto. At S_w = 1.13 an observed steep increase in AF in the $\geq$ 3 μm-OPC size bin indicates droplets only grew larger
than 3 μm at this S_w. Compared to the ammonium nitrate measurements performed at Zurich, a delayed activation is observed.
This is expected because of the decrease in ambient pressure, which results in shorter residence times, and the less pronounced
hygroscopicity of ambient particles at the JFJ. The signal visible in the $\geq$ 4 μm-OPC size bin comes from INPs, which nucleate
and grow to ice crystals at $S_w \geq$ 1.028 ($S_i \geq$ 1.378). This validates the calculations above that at S_w = 1.04 droplets cannot
240   grow to sizes $\geq$ 4 μm but ice crystals can supporting the use of the $\geq$ 4 μm size bin to detect ice crystals.
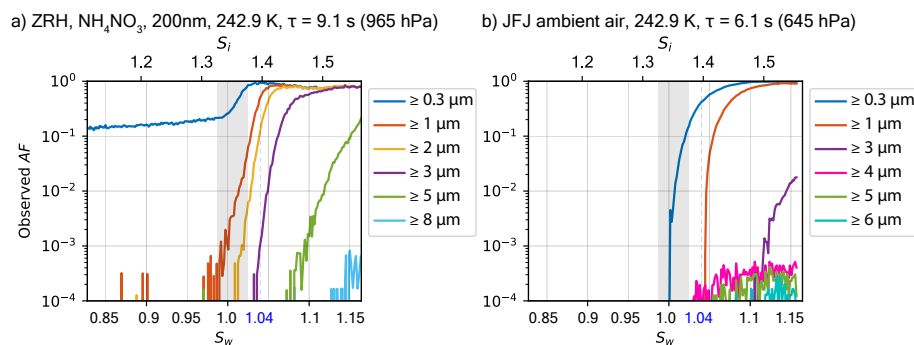
Figure 6. Activation curve at T = 243 K for a) ammonium nitrate, sampled at Zurich and b) ambient air, sampled at JFJ during an period with enhanced INP concentrations. Both measurements were performed with HINC-Auto with an identical injector position, but resulted in a shorter particle residence time (τ) at the JFJ compared to Zurich because of the reduced ambient pressure. Grey shading refers to chamber uncertainty (see Section 3.1 for details).

False positive counts can arise from large particles other than ice nucleated on an INP. Dominant false positives arise from frost grown on inner chamber surfaces which break off and get carried with the prevailing airflow until exiting the chamber, where they are detected by the OPC. To assess and correct the measurements for these false counts, before and after a sampling period of 15 min a background measurement of 5 min is performed. During the background measurement the sample air is directed through a HEPA filter before being sampled in the chamber. The mean time-normalized background counts before and after each INP measurement in the $\geq$ 4 μm bin are subtracted from the $\geq$ 4 μm-OPC counts during the INP measurement before the conversion to std L min^{-1}. The limit of detection (LOD) is calculated as follows:

$$LOD = \frac{\sqrt{\sum BG\ counts}}{\sum N_{BG\ samples}} \frac{60}{V t_{OPC}} \qquad [LOD] = \text{std L min}^{-1} \qquad (1)$$

Where $\sum BG\ counts$ is the sum of the background counts before and after the measurement, $\sum N_{BG\ samples}$ is the total number of OPC intervals with duration t_{OPC} in seconds used to count all background counts before and after the measurement, and V is the volume flow through the OPC, here V = 2.83 std L min^{-1}. The stated LOD provides a 62.3% (1 σ) confidence interval. The minimum detectable concentration (MDC, 1 count) for a INP measurement with a sample flow rate of 0.283 std L min^{-1} over 15 minutes is 0.236 std L^{-1}.

3 Results

3.1 Accuracy

Four main parameters characterize the INP concentration measured: temperature, supersaturation, particle count and volume flow. The thermocouples have an uncertainty of $\pm$ 0.1 K and are calibrated measuring the melting of H$_2$O and Hg, in close agreement with the ITS-90 (the official protocol of the international temperature scale). The temperature variation across the

warm and cold wall is $\pm$ 0.35 K and $\pm$ 0.25 K at T = 243 K and S_w = 1.04, respectively. However, on each wall only the
two thermocouples close to the injector and the chamber outlet are used to calculate the mean wall temperature. The variation
therefore decreases to $\pm$ 0.14 K and $\pm$ 0.05 K at T = 243 K and S_w = 1.04 on the warm and cold wall, respectively. In either
case, the temperature increases in the direction of the air flow, because of the parallel-flow setup of the cooling liquid (see
Figure 2b). Therefore, the resulting total temperature variation in the center between the two cooling walls is $T \pm$ 0.24 K. The
accuracy of the supersaturation within HINC-Auto relies indirectly on the measured temperature, too, since the wall tempera-
tures define the supersaturation. In addition, the vertical position of the aerosol layer determines the T and S experienced by
the particles. Thus, the temperature uncertainty translates together with the maximal displacement of the particles within the
center lamina with a sheath to sample flow ratio of 9:1 resulting in a supersaturation uncertainty of S_w + 0.007 and - 0.009 and
a total temperature uncertainty of $\pm$ 1.11 K at nominal T = 243 K and S_w = 1.04. This corresponds to a experienced range of
$1.03 \leq S_w \leq 1.05$. The used OPC can distinguish and size bin 4995 individual particles per second with an accuracy of $\pm$ 10%
to the calibrated aerosol. The sheath air MFC has a standard deviation of σ = 1.07%, and the MFC downstream of the OPC a
standard deviation of σ = 0.25%. The CPC used for validation experiments has a counting uncertainty of $\pm$ 10% which yields
in a relative uncertainty in the reported AF of $\pm$ 14%.

3.2 Validation

An overview of the validation of HINC-Auto is shown in Figure 7. Ammonium sulfate (($NH_4)_2SO_4$), ammonium nitrate
(NH_4NO_3) and sodium chloride (NaCl) were sampled from a aqueous solution with 0.1 mol L^{-1}, atomized, dried using a dif-
fusion dryer to $S_w \leq 0.002$ at 20 °C and size selected to a mobility diameter d_m = 200 nm by a differential mobility analyzer
(DMA, TSI 3082, sheath flow set to 8 L min^{-1}, sample flow 1.3 L min^{-1}). A CPC (TSI 3878) measured the particle con-
centration in parallel to HINC-Auto to obtain AF. The particle concentration was targeted to 200 cm^{-3}. The injector position
in HINC-Auto was kept constant yielding in between τ = 8 (273 K) and 10 seconds (218 K) residence time, depending on
the temperature of the mid lamina. The experiments were conducted with constant mid lamina temperature while the super
saturation is increased with ΔS_w = 0.02 min^{-1}. The onset of activation in the 1 µm-channel is reported for when the signal
exceeds the background noise levels.

NH_4NO_3 is used to test cloud droplet formation at $T \geq 235$ K and homogeneous freezing of solution droplets at $T \leq 235$
K. Cloud droplet formation within the uncertainty range of HINC-Auto is detected at water saturation for 235 K $\leq T \leq$ 263
K. At the lower end of the temperature spectrum, the activation onset is more sudden (see Figure A5) and starts lower than
water saturation. For homogeneous freezing at 233 K the activation is steep at S_w = 0.97, 0.017 lower than the parameterized
homogeneous freezing onset of solution droplets for d_0 = 200 nm and J = 10^{10} $cm^{-3}s^{-1}$ (Koop et al., 2000b), but within
the theoretically reported value considering uncertainty. At 228 and 222 K, the measured activation agree well with the the
parameterized homogeneous freezing onset. The deliquescence of ammonium sulfate (($NH_4)_2SO_4$) was observed at S_w = 0.88

(at 234.9K) to 0.86 (at 245.1K) within the range of uncertainty of literature values (Braban et al., 2001) as shown in Figure 7. The deliquescence of sodium chloride (NaCl) lies within the range of uncertainty of measured values by Koop et al. (2000a).
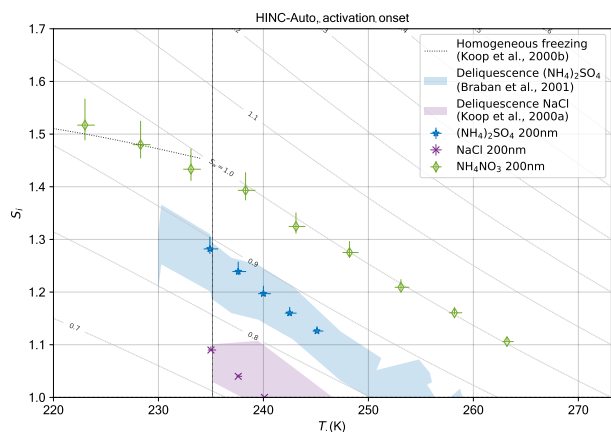
Figure 7. Data from experiments in HINC-Auto and comparison to values from literature for cloud droplet formation and homogeneous freezing onset with ammonium nitrate, and deliquescence of ammonium sulfate and sodium chloride. Reported is the activation onset when the signal increases above the background noise levels. Dashed line: homogeneous freezing onset of solution droplets for $d_0 = 200$ nm and $J = 10^{10}$ cm^{-3}s^{-1} (Koop et al., 2000b).

3.2.1 Improvement in precision

295 Figure 8 shows the activation curves of ammonium nitrate experiments at $T = 233$ K performed with HINC-Auto compared to measurements performed with HINC. The sample preparation is as described above for both chambers and the injector position was chosen to result in residence times of $\tau \approx 9$ seconds. The sheath to sample flow ratio was 12:1 for both chambers. HINC-Auto shows an improved reproducibility compared to HINC. For measurements in the field with HINC, a defined supersaturation (e.g. $S_w = 1.04$), temperature and OPC-size bin (e.g.≥ 4 µm) is used to quantify INPs. Therefore, fluctuations
300 in the activation reproduciblity of the ≥ 4 µm size bin can lead to uncertainties in INP concentrations. In the example of HINC, this is equivalent to more than one order of magnitude, thus an improved repeatability improves the quality of the INP measurements. In addition, particle sedimentation, as expected by theory (see Section below), is visible in the activation curves of HINC-Auto at $S_w \geq 1.02$ (see Section 3.2.2).
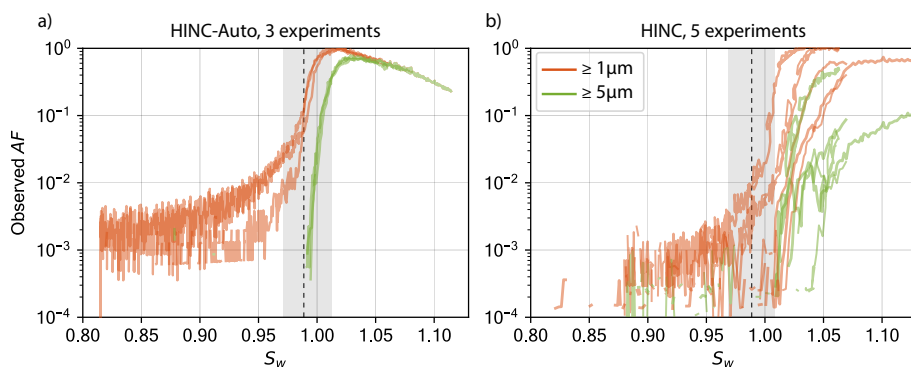
Figure 8. Activation curves of ammonium nitrate in HINC-Auto (a) and HINC (b) at T = 233K with identical particle residence times. of $\tau \approx 9$ sec.; the vertical dashed line indicates the expected homogeneous freezing onset of solution droplets for d_0 = 200 nm and $J =10^{10}$ cm^{-3}s^{-1} (Koop et al., 2000b). Sizes indicate what fraction of all particles entering the chamber grow to or beyond the indicated size. Grey shading refers to chamber uncertainty (see Lacher et al. (2017) for details on HINC and Section 3.1 for details on HINC-Auto).

3.2.2 Sedimentation study

305 The 2D diffusion model can also be used to calculate the diffusional growth of liquid and solid hydrometeors and their subsequent sedimentation characteristics. An example is given in Figure 9a and compared to an experiment of silver iodide (AgI, Figure 9b) at T = 243 K with a residence time of τ = 13.7 sec at p = 965 hPa. AgI samples were prepared by aqueous solutions of 0.01 mol L^{-1} of potassium iodide and silver nitrate, where the silver nitrate solution was slowly added to the potassium iodide under constant stirring. This procedure favors the formation of β-AgI over α-AgI (Brauer, 1965). After resting for 60

310 min, the top 80% (consisting only of a clear solution) of the yellow suspension was decanted and the equivalent of removed volume was added in ultra pure water. A brief swivel lofted the settled precipitate. The decanting procedure was repeated twice. The suspension was atomized, dried using a diffusion dryer to $S_{\text{w}} \leq 0.008$ at 20 °C and size selected to d_m = 100 nm by a DMA. For the simulation, the ice active fraction (*FF*) has been set to 15% for the simulation to agree best with the *FF* observed. The *FF* depends on the fraction of ice active β-AgI particles within all particles (Marcolli et al., 2016), which also

315 contain ice inactive α-AgI particles and cannot be deduced by the 2D diffusion model. The model uses the size distribution after the DMA measured by a Scanning Mobility Particle Sizer (SMPS) setup (DMA, TSI 3081, with CPC, TSI 3772) as input for the particle initial sizes and also places the particles (N = 1000 for each, INPs and CCN) at uniformly distributed vertical positions within the sample lamina. The model assumes instant activation of the particles as soon as ice or water saturation are reached. Also Köhler-theory is not implemented. Ice crystals are assumed to be spherical.

320
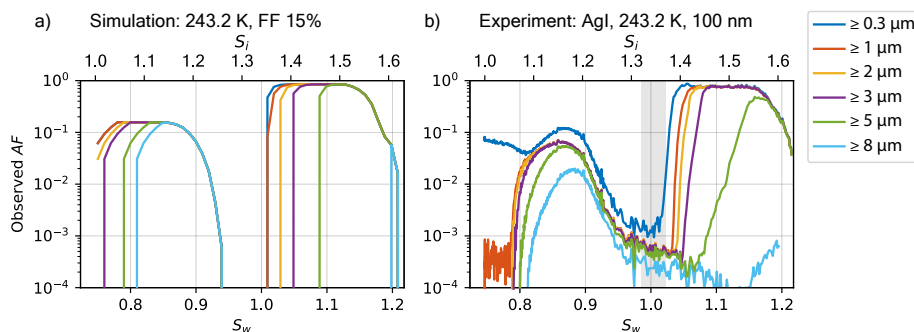
Figure 9. a) Simulated activation curve with a frozen fraction *FF* of 15% and b) measured activation curve of 100 nm silver iodide (AgI) particles, both at $T = 243$ K, with a particle residence time of $\tau = 13.7$ sec at $p = 965$ hPa. Sizes indicate what fraction of all particles entering the chamber grow to or beyond the indicated size. Grey shading refers to chamber uncertainty (see Section 3.1 for details).

The model can capture the general trend of the experiment. The rapid onset of ice formation at $S_w \leq 0.8$ is not reproduced because this depends on the nucleation rate of the substance, which is neither parameterized nor simulated using molecular dynamics or similar approaches. However, the simulation demonstrates an upper bound of possible sizes, which is in agreement with the experiment. Where the ice growth is limited by the amount of supersaturation required for diffusional growth, e.g. at

325    $S_w \geq 0.81$, the transition of ice crystals growing to a size ≥ 8 μm is reproduced well. The sedimentation of the ice crystals is observed at $S_w \geq 0.87$ while the simulation predicts $S_w \geq 0.86$. The onset of liquid droplets is identical in the experiment for sizes ≤ 3 μm, and delayed for larger sizes. Water vapor depletion is not likely the cause because running the experiment with a sample concentration of 20 or 1200 particles cm^{-3} compared to the original 200 particles cm^{-3} did not alter the slow growth of hydrometeors ≥ 5 μm. We expect the delay to be present because of the missing implementation of Köhler-theory.

330   The *AF* in the experiment as well as in the simulation is leveling off at $AF = 0.85$ for $1.02 \leq S_w \leq 1.13$. Ice crystals (≈ 15 % in the experiment) and supercooled droplets are continuously formed at these supersaturations, but ice crystals grow to such large sizes that they sediment and are not detected at the outlet anymore. The sedimentation of droplets is observed delayed at $S_w \geq 1.16$ compared the model output at $S_w \geq 1.13$. This is likely a result of the delayed onset of liquid droplet formation seen in the experiment. While increasing the supersaturation the droplets remain too small, thus their size-dependent settling

335   is delayed, too.

3.2.3   INP measurement

To assess HINC-Auto's capability of fully automated INP measurement, Nx Illite was sampled in a controlled laboratory environment. The goal of this experiment is to assess how reliablly INPs can be detected over different INP concentrations and what their impact is on the ice layer endurance, thus deciding which rewetting intervals are needed and to test the overall

340   automation of the chamber. HINC-Auto was, therefore, run autonomously except for a change in when to trigger the rewetting sequence. Using the software user interface, a command was sent to the chamber after the chamber was presumed to have run dry. This has been inferred based on the decay of the reported INP concentrations. For the experiment, Nx Illite was dry

dispersed by a rotating brush generator (PALAS, RBG 1000) into a stainless steel aerosol chamber with V = 2.78 m³, initially filled with dry, pure nitrogen. The volume within the aerosol chamber was actively stirred with a gold-plated fan (30 cm

345   diameter). The observed particle number size distribution was 30 - 1000 nm (see Figure 10a). A common sample line from the aerosol chamber feeds a two way flow spitter, which connects HINC-Auto and a CPC (TSI 3778) using tubing with identical length and diameter. A burst of Nx Illite was initially added to the aerosol chamber and continuously diluted by sampling 0.883 std L min^{-1} (0.283 std L min^{-1} for HINC-Auto and 0.6 std L min^{-1} for the CPC) and adding 1.0 std L min^{-1} of dry N$_2$. An additional bypass valve allowed to vent the excess N$_2$ before entering the aerosol chamber. HINC-Auto was run at mixed-

350   phase cloud condition at T = 243 K and S_w = 1.04 to sample in the immersion freezing mode with a sheath to sample flow ratio of 9:1 and a residence time of $\tau \approx 8$ seconds. The chamber measured intervals of sample aerosols for 15 min and filtered background for 5 minutes. Figure 10b shows the measured INP and particle concentrations during the course of the experiment. Since the initial burst of Nx Illite is suspended in dry, inert nitrogen, it is expected for the ice active fraction to remain fairly constant or decrease slightly over time. A slight decrease is expected when larger particles, which tend to be more ice active because of the higher surface area, sediment within the tank sooner than small particles. A SMPS setup (DMA, TSI 3082, with

355   CPC, TSI 3878) measured the size distribution at the beginning of the experiment and after 62 hours (see Figure 10a). The for the initial scan (solid line) the sheath flow set to 5 L min^{-1}, and for the second scan to 2 L min^{-1} (dashed line). Both measured size distributions were similar with a small shift towards larger particles for the later scan. This is contradicting our assumption and the lower sheath flow rate of the DMA for the second compared to the first measurement could be the reason.

360   The measured INP concentrations show a systematically repetitive trend: After each rewetting sequence the ratio between particle and INP concentration is approximately 1:1000. During the operation of the chamber the ratio remains fairly constant and decreases after some time. We expect the decrease to coincide with the depletion of the top wall ice layer. The higher the particle number concentration (N), the sooner the decrease is expected (due to consumption of water vapor mass), and observed. For atmospheric relevant conditions at the JFJ with 400 cm$^{-3} \leq N \leq$ 1000 cm^{-3} the drop occurs after 8.5 hours,

365   for 95 cm$^{-3} \leq N \leq$ 200 cm^{-3} after 13 hours. N is expected to contribute more in water vapor depletion than the INP number concentration because approximately 1000 times as many particles grow to liquid droplets of a size of $\approx$ 1.3 µm than INPs grow to $\approx$ 4.7 µm. At particle concentrations $\leq$ 30 cm^{-3} and INP concentrations $\leq$ 30 std L^{-1} the INP concentration starts to show noise which increases in relative magnitude with decreasing particle concentrations. A running mean of 4 subsequent measurements decreases the noise and allows the particle to INP ratio to remain until $\approx$ 6 INP std L^{-1}. Based on the above

370   experiment, we chose a rewewtting time of 10 hours for field applications (Section 3.3).
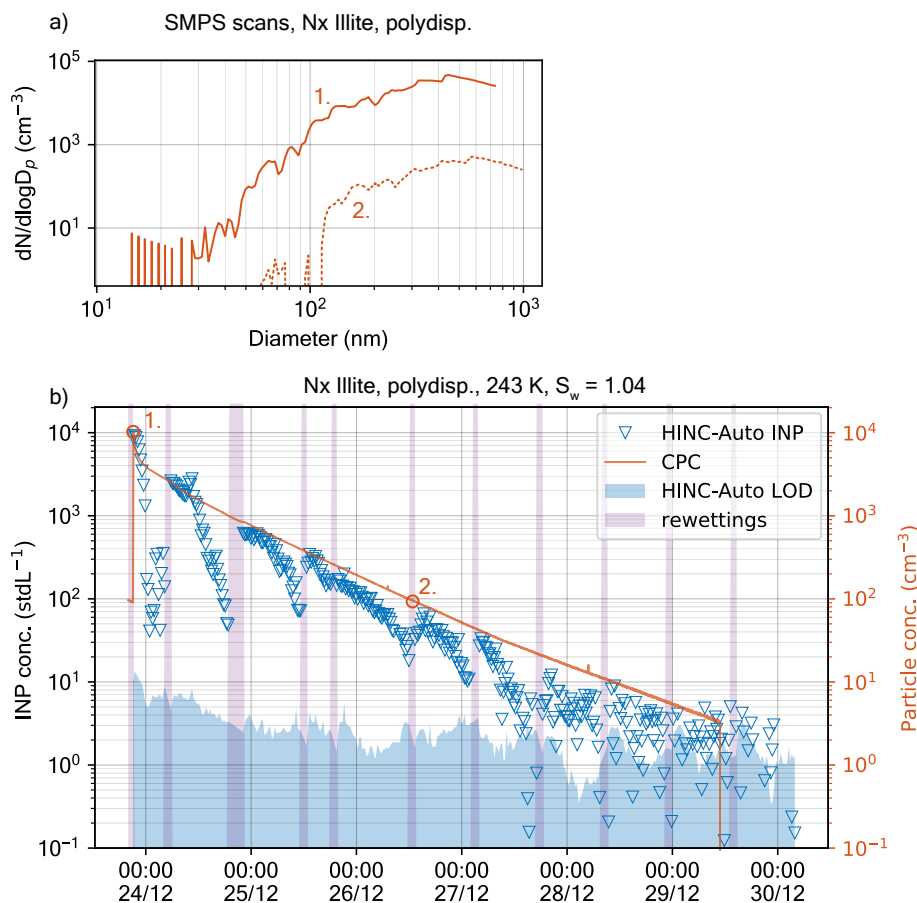
Figure 10. INP concentration in HINC-Auto as a function of time and Nx Illite particle concentration. a) SMPS retrieved particle size distribution at time 1 (solid line) and 2 (dashed line). The DMA sheath flow was set to 5 (solid line) and 2 L min^{-1} (dashed line). b) Measured INP and particle concentrations within the aerosol tank.

3.3 Application

The automation of HINC-Auto was tested during a field campaign in August 2019 on the JFJ. In this time, HINC-Auto was operational for 169 out of the 177 available hours (95.5%) and measured 463 measurements-background sequences of a duration of 20 minutes each (see Figure 11a). The maximum measurement coverage with HINC in a time window of 177 hours during

375 previous field campaigns was 191 measurement sequences (see Lacher et al., 2018), also 20 minutes in duration (103 hours, 58%, see Figure 11b). The automation shows a clear improvement in the continuity of the measurements. However, during the field campaign the LOD of HINC-Auto was appreciably higher than the LOD of HINC during previous field campaigns (median LOD HINC-Auto: 3.1 std L^{-1}, HINC: 1.25 std L^{-1}). Design changes implemented in a second field campaign started in February 2020 resulted in a median LOD of 1.37 std L^{-1}. In the first month the chamber was operational for 698 out of

380 720 available hours (97.0%). A broken membrane of the recirculating pump caused 10 hours of downtime, the measurement of

ramps at the beginning of the campaign resulted in 7 hours when the chamber was not performing INP measurement sequences. The remaining 5 hours were due to multiple software glitches which were fixed. In March 2020, HINC-Auto was operating more reliably with a total downtime of 3 hours because of software bugs. Bug fixes were implemented and let to an operation without any downtime in April 2020. Continuous INP measurements of HINC-Auto at the JFJ are planned to proceed. Live

385   data can be accessed at https://www.psi.ch/en/lac/projects/last-72h-of-aerosol-data-from-jungfraujoch.
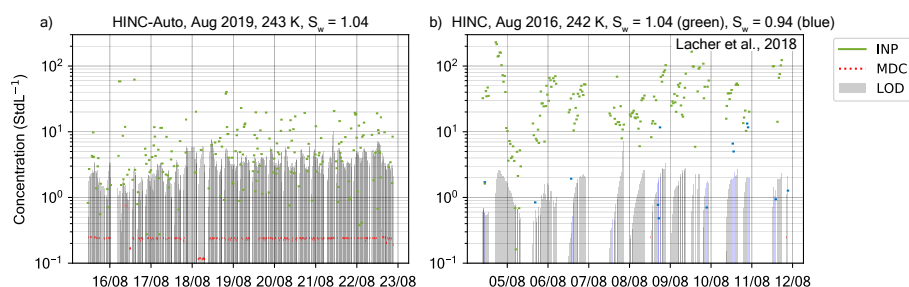
Figure 11. INP measurements at the JFJ over a period of 7 days with a) HINC-Auto at T = 243 K and S_w = 1.04 and b) HINC at T = 242 K and S_w = 1.04 (green markers) or S_w = 0.94 (blue markers) (see Lacher et al., 2018). Green/blue markers indicate the ambient INP concentration, the grey bar indicates the limit of detection (LOD) with a 62.3% (1 σ) confidence interval, red markers indicate measured INP concentrations below the minimum detectable concentration (MDC, 1 count during the sampling time). Every grey bar with a corresponding green/blue/red dot represents one measurement.

4   Conclusions

In this study the automated Horizontal Ice Nucleation Chamber (HINC-Auto) is presented, a continuous flow diffusion chamber to measure atmospheric ice nucleating particle number concentration. During a first field campaign, the chamber was operational fully autonomously for 95% of the time. Over a 90 day period of a second field campaign, HINC-Auto measured INP

390   autonomously for 97% of the time. This time includes INP sampling time as well as periodically reoccurring rewetting procedures. To realize full autonomous operation, the rewetting procedure in HINC was automated. In HINC-Auto, a peristaltic pump remoistens the filter paper that coats the top (warm) wall within the chamber while a linear motor tilts the chamber thereby allowing excess water to drain. The bottom wall passively wets through diffuson of vapour from the cold wall. To maximize the sampling time, the duration of the rewetting procedure was reduced by reducing the warming and cooling time of the

395   chamber by using a lower thermal mass for the chamber walls. This was done by using aluminium compared to copper and by shortening the chamber. To maintain a well developed relative humidity profile within the sampling section in the shortened chamber, the sheath air is precooled using heat sinks mounted on the cold, bottom wall. Besides the automation, improvements to the flow uniformity were achieved by the integration of a mesh. The resulting activation curves during experiments with relative humidity ramps are steeper in expectation to theory and show a better reproducibility. In addition, the experiments

400   match the predictions of a 2D diffusion model to a high degree. Experiments with HINC-Auto for cloud droplet formation and homogeneous freezing onset with ammonium nitrate, and deliquescence of ammonium sulfate and sodium chloride showed

good agreement with values found in literature. HINC-Auto is currently deployed for long-term continuous measurements of INP at JFJ and analysis after a year of data collection will be presented in a follow up study.

Code availability. The code used for simulations presented here is available upon contacting the authors.

405 *Data availability.* The data presented in this publication will be made available at DOI: 10.3929/ethz-b-000429220. Note by authors: Data will be made available upon publication

Appendix A

A1 CFD simulations

The CFD simulations were performed using Siemens PLM STAR-CCM+ © V13.04.010. A grid convergence study was con-
410 ducted prior to the simulations. A 96% convergence of the flow field was observed for the following settings, which were used for all subsequent studies. A tetrahedral mesh with a total count of 9.5×10^6 cells was generated with the surface remesher option and 5 prism layers with a stretching of 1.3. The base mesh size was set to 2 mm with a refinement of 0.25 mm around the injector and the heat sinks and a further refinement of 0.1 mm in the vicinity of the injector's slit. The physics model consisted of 3D turbulent Reynolds-Averaged Navier-Stokes equations, k-ω turbulence model, Lagrangian multiphase with water vapor
415 and air, steady-state, segregated fluid enthalpy, ideal gas, and gravity. Convergence was observed after ~ 2000 iterations with energy-residuals $< 10^{-5}$ as criterion. An unsteady simulation showed no instationary flow behavior and was consistent with the steady-state solution.

A2 Particle Image Velocimetry
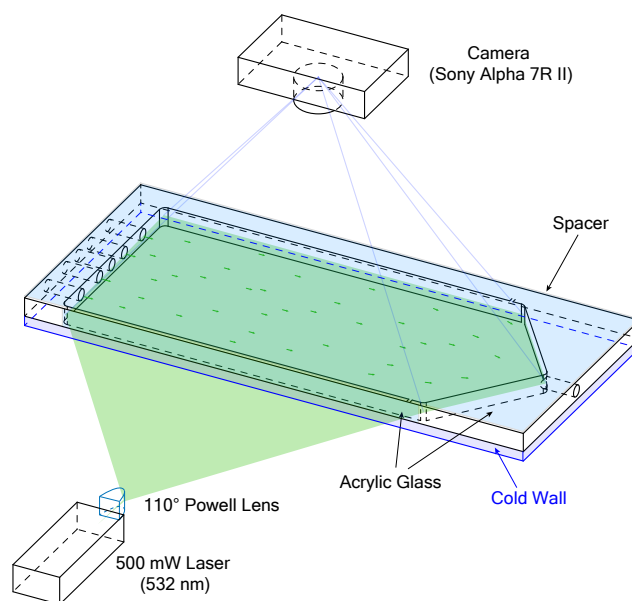
Figure A1. Schematic of the particle image velocimetry experiment with HINC.

Particle image velocimetry (PIV) has been used to validate the CFD-simulations. Figure A1 illustrates the experimental set-

420 up using HINC. Dry Nx Illite size-selected particles to a mobility diameter $d_m = 400\ nm$ have been used as tracer. Two experiments were conducted: first, the chamber without the injector. The particles were added to the sheath air. The goal was to sample the overall flow within HINC and deduce the 2D-velocity field. The injector was installed for the second experiment. Here, the areas of interest were to study the impact of the injector on the base-flow within the chamber, as well as the trajectories of non-sedimentating particles as they exit the injector. All results are for the purpose of validating the

425 CFD-simulations. The image sequences were recorded by a SONY Alpha 7R II with a resolution of $\Delta^2_{low} = 3840 \times 2160$ pixel and $\Delta^2_{high} = 1920 \times 1080$ pixel. The camera captured images at $f_{low} = 25$ fps and $f_{high} = 100$ fps. A 500 mW-laser-diode with a wavelength of $\lambda = 532\ nm$ was used as continuous light source. The laser beam is deflected with a K9 110 degree Powell lenses into a straight line, and oriented such, that it illuminates a horizontal plane. The laser's vertical position was controlled by a stepper-motor and could be adjusted with a resolution of 0.05 mm. This allowed to scan the entire chamber

430 and produce a 3D matrix containing the xy-planar velocity components. The laser-facing wall of the CFDC's spacer has been replaced by a planar transparent acrylic glass to allow the laser beam to pass. Also, the top cooling wall has been replaced by clear acrylic glass to allow the camera to capture the illuminated particles. The lower wall was chilled to 279.6 K, while the top acrylic's temperature was at ambient (297 K). The resulting temperature difference of 17.4 K is identical to when the chamber is operated at $T = 243$ K and $S_w = 1.04$. It is assumed that the absolute temperature has a minor impact on the flow,

435 while it is important to mimic the relative temperature differences since it represents the difference in fluid densities. The post-

processing has been done using PIVlab (Thielicke and Stamhuis, 2014). Fast Fourier Transform linear window deformation technique was used as PIV algorithm with an interrogation area of 128 pixel and a step size of 64 pixel. A second pass an interrogation area of 64 pixel and a step size of 32 pixel followed. Figures A2 and A3 compare the flow field retrieved from the PIV experiments with the CFD-simulations. For the PIV experiments low-settings were used to capture the flow of the

440   entire fluid domain, whereas the $high$-settings were used to extract flow features where the low-settings failed to produce a valid output. Nevertheless, in the areas after the sheath flow outlets the flow velocity was too high to be captures with the $high$-settings. Also, close to the spacer walls, no velocity information could be computed, because of the Fast Fourier Transform window deformation technique. Quantitatively the CFD simulations are able to capture the flow structures measured during the experiment. Quantitatively, the correlation of the u, w-velocity components all voxels resolved by the experiment with the

445   u, w-velocity components of the simulation with identical locations were $r_{HINC} = 0.94$ and $r_{mesh} = 0.95$ for the experiment without and with mesh, respectively. Least correlation was observed in the areas of the sheath flow jets where high flow velocities are present. Also, the simulated particle trajectories were qualitatively stringent with the experiment. Therefore, the CFD simulations were deemed valid.
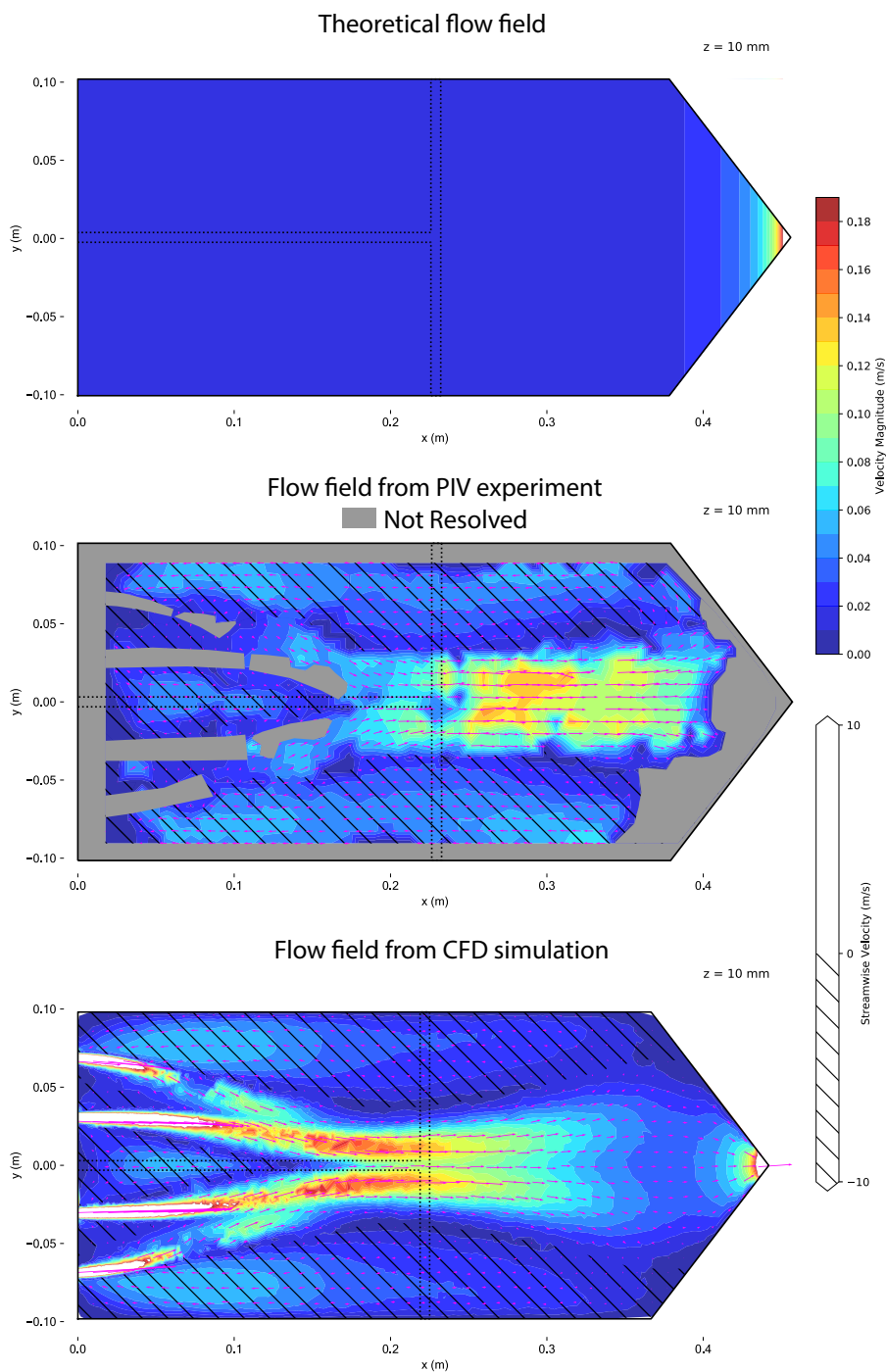
Figure A2. Contour plot of flow velocities magnitudes at a horizontal plane of the HINC cavity at mid-height. The chamber is set to $T = 243$ K and $S_w = 1.04$. Theoretical flow field (top), flow field measured using PIV (center) and simulated flow field from CFD (bottom). Arrows indicate flow direction, the hatching marks regions with reversed flow. The dashed line represents a possible position of the injector.
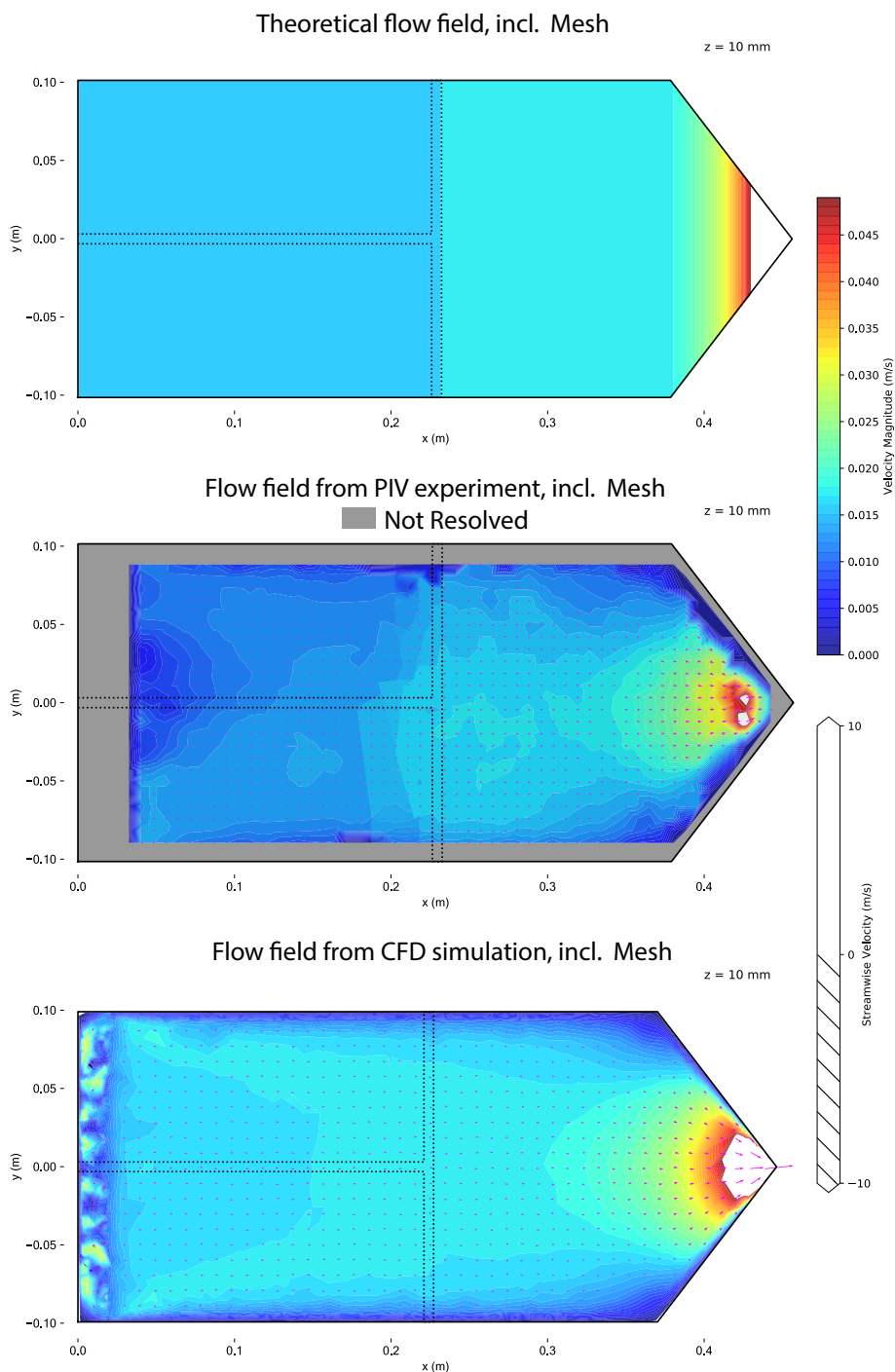
Figure A3. Contour plot of flow velocities magnitudes at a horizontal plane of the HINC cavity at mid-height including a mesh installed at $x_{inj} = 0.022\ m$. The chamber is set to $T = 243$ K and $S_w = 1.04$. Theoretical flow field (top), flow field measured using PIV (center) and simulated flow field from CFD (bottom). Arrows indicate flow direction, the hatching marks regions with reversed flow. The dashed line represents a possible position of the injector.

A3   2D-Diffusion model

450   A numerical diffusion model has been developed to simulate the water vapor saturation field within HINC-Auto. The output of the model is a 2D vertical plane of a horizontal CFDC and its prevailing temperature and water vapor saturation field. Assuming a two-dimensional flow along the chambers length, for the prevalent conditions with Reynolds number $Re = 6.82 \times 10^2$ between two long plates the analytical solution of the Navier–Stokes equations describes a Poiseuille flow according to equations (A1) and (A2):

455    $$u_{\infty_{bulk}}(x) = \frac{\dot{V}}{A_{yz}(x)} \tag{A1}$$

$$u(x,z) = \frac{3}{2} u_{\infty_{bulk}}(x) \left(1 - \frac{\left(z - \frac{h}{2} \right)^2}{\left(\frac{h}{2} \right)^2} \right) \tag{A2}$$

Where x, y, z are the coordinates along the length, width and height of the chamber. The origin is located on the bottom cooling wall where the sheath-air enters at mid-width. $u_{\infty_{bulk}}(x)$ is the bulk velocity along the chamber's length, V is the preset volume flow of air, $A_{yz}(x)$ is the vertical cross-section of the chamber's cavity which varies along the length of the

460   chamber, u is the stream wise velocity component and h is the total height of the chamber. According to equation (A2) the center lamina has a 50% higher flow velocity than the bulk flow velocity. The particle's theoretical residence time τ_{theory} is calculated using equation (A3):

$$\tau_{theory}(x_{inj}) = \int\limits_{x_{inj}}^{x_{outlet}} \frac{x}{u_{\infty_{bulk}}(x)} dx \tag{A3}$$

Where x_{inj} is the the injector's x-position and the outlet's x-position x_{outlet}.

465   In CFDCs the temperature and water vapor concentration of the air flow equilibrates from their initial states to form a water vapor supersaturated region. To calculate the sedimentation of particles as well as estimate the particle's final size the two underlying diffusion processes have to be described. Firstly, the heat flux between the warm and cold wall. We assume in accordance to Saxena et al. (1970) no radiation. Although the Nusselt number $Nu = 15.3$ propose otherwise, the calculations are simplified by considering thermal conduction only and neglecting the forced convection. The heat conduction within the

470   ice layer can be neglected (Biot number $Bi = 7.27 \times 10^{-5}$). The calculated numbers are computed for HINC-Auto, the corresponding values of the chamber of Rogers (1988) are $Nu = 22.3$ and $Bi = 1.14 \times 10^{-4}$ for $T_{mid} = 253.15 \ K$ and $\dot{V} = 4$ std L min^{-1}. Besides, the latent heat released or absorbed by the particles or by the wall's ice layer is neglected for calculation of the chamber's internal temperature field. The former is taken into consideration during the diffusion growth calculations (Rogers and Yau, 1996). This leads to the diffusion of heat in air by changing their kinetic energy, according to the heat equation (A4)

475   (?):

$$\frac{\partial T_{air}}{\partial t} = \frac{\lambda_{air}}{c_{p_{air}} \rho_{air}} \frac{\partial^2 T}{\partial x^2} \tag{A4}$$

Where T_{air} is the temperature of the air, t is the temporal variable, λ_{air} is the thermal conductivity of air, $c_{p_{air}}$ is the heat capacity of air at a constant pressure, ρ_{air} is the density of the air and x is the spatial coordinate.

The second diffusion process is the diffusion of water vapor according to Fick's law (Fick, 1855) in equation (A5):

$$\frac{\partial \mu_{H_2O}}{\partial t} = D_{H_2O/air} \frac{\partial^2 \mu_{H_2O}}{\partial x^2} \tag{A5}$$

Where C_{H_2O} is the concentration of water vapor, $D_{H_2O/air}$ is the diffusivity of water vapor in air and μ_{H_2O} is the chemical potential of the water vapor.

Saxena et al. (1970) states in equation (A5) to use the water vapor concentration C_{H_2O} instead of the chemical potential, yet, it was chosen to use the water vapor partial pressure e in accordance with Rogers (1988). Fundamental theory often suggests the diffusion to be driven by the difference in chemical potential (Sutherland, 1905; Einstein, 1905). Diffusion based on partial pressure or concentration results in different supersaturations than diffusion based on chemical potential. This has has a profound impact on the operating conditions in CFDCs, since the partial pressure is a function of the concentration as well as of the temperature, as seen in the rearranged ideal gas law, (A6), and changes the supersaturation in a non-linear fashion:

$$e = \frac{C_{H_2O}RT}{M_{H_2O}} \tag{A6}$$

For the 2D-diffusion model, both heat, and diffusion equations are solved numerically using the forward Euler method. The velocity is prescribed using equation (A2). The 2D fluid domain is modeled using a mesh with a grid spacing of 1 mm (7500 nodes in total). The steady state simulation converged after ≤ 100 iterations. Buoyancy has been neglected because it showed to have minor effect on the supersaturation field within horizontal CFDC. The model output has been compared versus a validated CFD simulation as visualized in Figure A4.
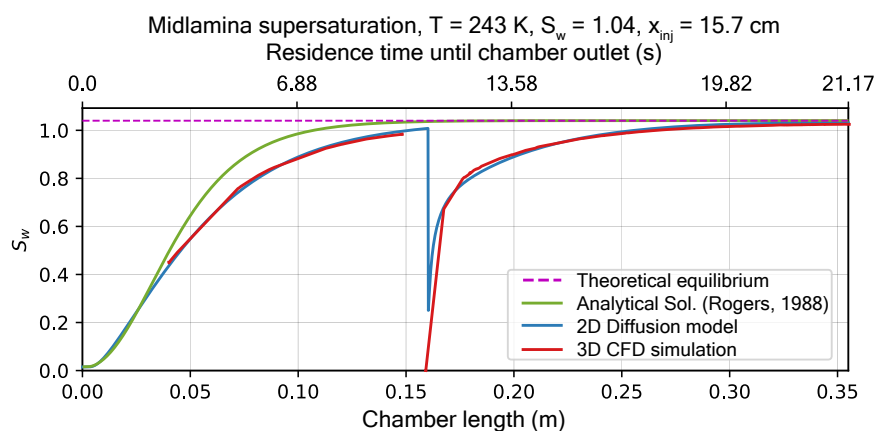
Figure A4. Comparison of the midlamina water supersaturation at $T = 243$ K, as calculated using the analytical formula (Rogers, 1988), simulated using the 2D-diffusion model and the 3D-CFD simulation.

495 **A4 Ammonium nitrate experiments**
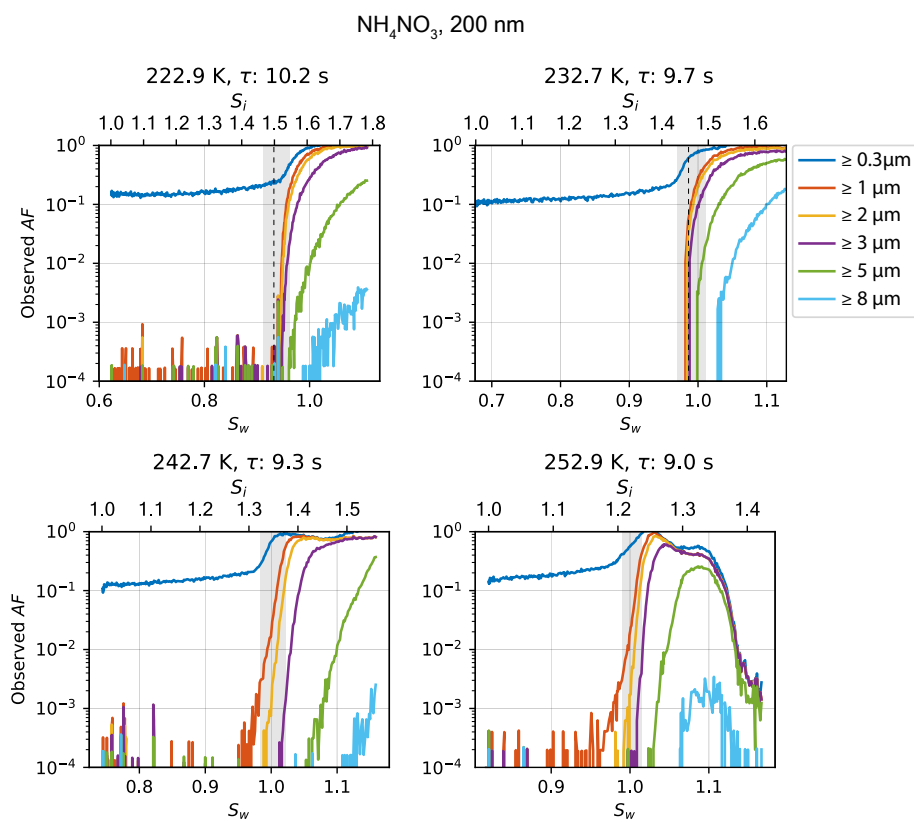
Figure A5. Relative humidity ramps showing the increase in *AF* during deliquescence and cloud droplet formation of 200 nm ammonium nitrate particles at various temperatures. Grey shading refers to chamber uncertainty (see Section 3.1 for details).

A5 Ammonium sulfate experiments
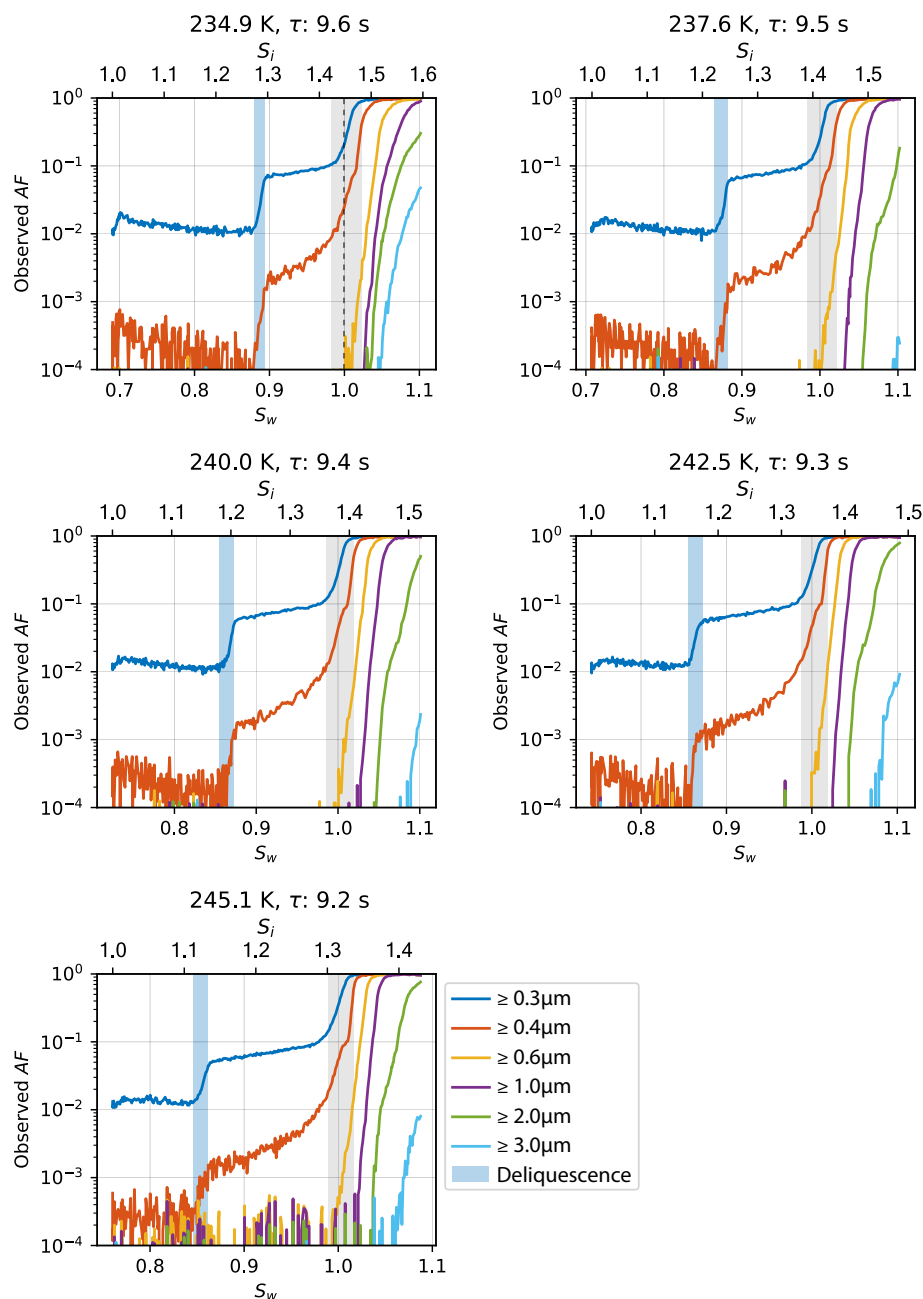
Figure A6. Relative humidity ramps showing the increase in *AF* during deliquescence and cloud droplet formation of 200 nm ammonium sulfate particles at various temperatures. Light blue shading highlights range of observed deliquescence, grey shading refers to chamber uncertainty (see Section 3.1 for details).

A6 Sodium chloride experiments
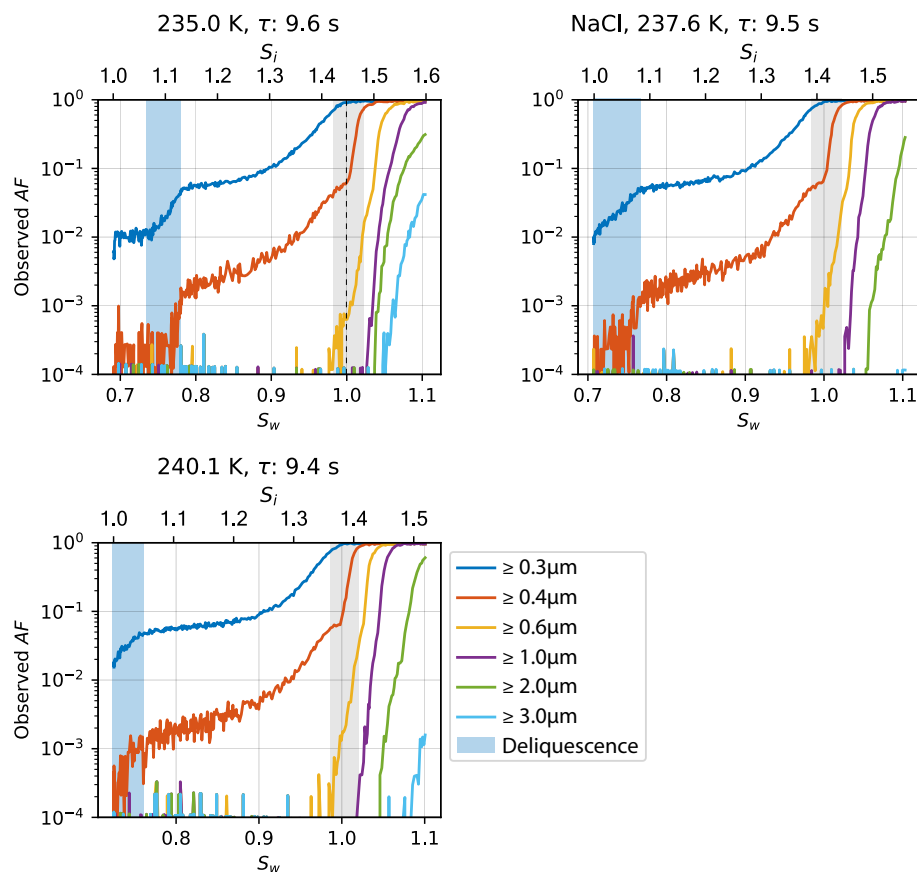
Figure A7. Relative humidity ramps showing the increase in *AF* during deliquescence and cloud droplet formation of 200 nm sodium chloride particles at various temperatures. Light blue shading highlights range of observed deliquescence, grey shading refers to chamber uncertainty (see Section 3.1 for details).

Author contributions. CB conducted experiments with input from ZAK. CB designed the HINC-Auto chamber with input from ZAK. CB designed and conducted PIV and CFD experiments. CB developed the 2D diffusion model. CB analysed the data and prepared the figures with input from ZAK. CB and ZAK interpreted the data. CB wrote the first draft of the manuscript with input from ZAK. ZAK conceived the idea, supervised the project and obtained funding.

Competing interests. The authors declare that they have no conflict of interest.

Acknowledgements. This research was funded by the Global Atmospheric Watch, Switzerland (MeteoSwiss GAW-CH+ 2018–2021). We thank Prof. Dr. Ulrike Lohmann for her support and enthusiasm. We acknowledge Jörg Wieder, Zane Dedekind, Dr. Fabian Mahrt, and Dr. 505 Carolin Rösch for useful discussions. For technical support and fabrication we would like to thank Dr. Michael Rösch and Marco Vecellio, whose expertise greatly helped to improve the instrument.

References

Al-Naimi, R. and Saunders, C. P. R.: Measurements of natural deposition and condensation-freezing ice nuclei with a continuous flow chamber, Atmospheric Environment (1967), 19, 1871–1882, https://doi.org/10.1016/0004-6981(85)90012-5, 1985.

510   Atkinson, J. D., Murray, B. J., Woodhouse, M. T., Whale, T. F., Baustian, K. J., Carslaw, K. S., Dobbie, S., O'Sullivan, D., and Malkin, T. L.: The importance of feldspar for ice nucleation by mineral dust in mixed-phase clouds, Nature, 498, 355–358, https://doi.org/10.1038/nature12278, 2013.

Beall, C. M., Lucero, D., Hill, T. C., Demott, P. J., Stokes, M. D., and Prather, K. A.: Best practices for precipitation sample storage for offline studies of ice nucleation 1, Atmos. Meas. Tech. Discuss., https://doi.org/10.5194/amt-2020-183, in review, 2020.

515   Boose, Y., Sierau, B., Isabel García, M., Rodríguez, S., Alastuey, A., Linke, C., Schnaiter, M., Kupiszewski, P., Kanji, Z. A., and Lohmann, U.: Ice nucleating particles in the Saharan Air Layer, Atmospheric Chemistry and Physics, 16, 9067–9087, https://doi.org/10.5194/acp-16-9067-2016, 2016.

Boucher, O., Randall, D., Artaxo, P., Bretherton, C., Feingold, G., Forster, P., Kerminen, V.-M., Kondo, Y., Liao, H., Lohmann, U., Rasch, P., Satheesh, S. K., Sherwood, S., Stevens, B., and Zhang, X. Y.: Clouds and Aerosols, book section 7, pp. 571–658, Cambridge University
520   Press, Cambridge, United Kingdom and New York, NY, USA, https://doi.org/10.1017/CBO9781107415324.016, 2013.

Braban, C. F., Abbatt, J. P., and Cziczo, D. J.: Deliquescence of ammonium sulfate particles at sub-eutectic temperatures, Geophysical Research Letters, 28, 3879–3882, https://doi.org/10.1029/2001GL013175, 2001.

Brauer, G.: Handbook of Preparative Inorganic Chemistry V2, v. 2, Elsevier Science, https://doi.org/10.1016/B978-0-12-395591-3.X5001-8, 1965.

525   Brubaker, T., Polen, M., Cheng, P., Ekambaram, V., Somers, J., Anna, S. L., and Sullivan, R. C.: Development and characterization of a "store and create" microfluidic device to determine the heterogeneous freezing properties of ice nucleating particles, Aerosol Science and Technology, 54, 79–93, https://doi.org/10.1080/02786826.2019.1679349, 2020.

Chou, C., Stetzer, O., Weingartner, E., Jurányi, Z., Kanji, Z. A., and Lohmann, U.: Ice nuclei properties within a Saharan dust event at the Jungfraujoch in the Swiss Alps, Atmospheric Chemistry and Physics, 11, 4725–4738, https://doi.org/10.5194/acp-11-4725-2011, 2011.

530   Conen, F., Rodríguez, S., Hüglin, C., Henne, S., Herrmann, E., Bukowiecki, N., and Alewell, C.: Atmospheric ice nuclei at the high-altitude observatory Jungfraujoch, Switzerland, Tellus, Series B: Chemical and Physical Meteorology, 67, 25 014, https://doi.org/10.3402/tellusb.v67.25014, 2015.

Cziczo, D. J., Ladino, L. A., Boose, Y., Kanji, Z. A., Kupiszewski, P., Lance, S., Mertes, S., and Wex, H.: Measurements of Ice Nucleating Particles and Ice Residuals, Meteorological Monographs, 58, 8.1–8.13, https://doi.org/10.1175/AMSMONOGRAPHS-D-16-0008.1,
535   2017.

Demott, P. J., Cziczo, D. J., Prenni, A. J., Murphy, D. M., Kreidenweis, S. M., Thomson, D. S., Borys, R., and Rogers, D. C.: Measurements of the concentration and composition of nuclei for cirrus formation, Proceedings of the National Academy of Sciences, 100, 14 655–14 660, https://doi.org/10.1073/pnas.2532677100, 2003.

DeMott, P. J., Sassen, K., Poellot, M. R., Baumgardner, D., Rogers, D. C., Brooks, S. D., Prenni, A. J., and Kreidenweis, S. M.: African dust
540   aerosols as atmospheric ice nuclei, Geophysical Research Letters, 30, 1732, https://doi.org/10.1029/2003GL017410, 2003.

Demott, P. J., Prenni, A. J., Liu, X., Kreidenweis, S. M., Petters, M. D., Twohy, C. H., Richardson, M. S., Eidhammer, T., and Rogers, D. C.: Predicting global atmospheric ice nuclei distributions and their impacts on climate, Proceedings of the National Academy of Sciences, 107, 11 217–11 222, https://doi.org/10.1073/pnas.0910818107, 2010.

Demott, P. J., Möhler, O., Stetzer, O., Vali, G., Levin, Z., Petters, M. D., Murakami, M., Leisner, T., Bundke, U., Klein, H., Kanji, Z. A.,

545   Cotton, R., Jones, H., Benz, S., Brinkmann, M., Rzesanke, D., Saathoff, H., Nicolet, M., Saito, A., Nillius, B., Bingemer, H., Abbatt, J. P.,
Ardon, K., Ganor, E., Georgakopoulos, D. G., and Saunders, C.: Resurgence in ice nuclei measurement research, Bulletin of the American
Meteorological Society, 92, 1623–1635, https://doi.org/10.1175/2011BAMS3119.1, 2011.

Dufour, L.: Ueber das Gefrieren des Wassers und über die Bildung des Hagels, Annalen der Physik, 190, 530–554, https://doi.org/10.1002/
andp.18621901203, 1862.

550 Einstein, A.: Ueber die von der molekularkinetischen Theorie der Waerme geforderte Bewegung von in ruhenden Fluessigkeiten sus-
pendierten Teilchen, Annalen der Physik, 322, 549–560, https://doi.org/10.1002/andp.19053220806, 1905.

Fick, A.: Ueber Diffusion, Annalen der Physik, 170, 59–86, https://doi.org/10.1002/andp.18551700105, 1855.

Garimella, S., Kristensen, T. B., Ignatius, K., Welti, A., Voigtländer, J., Kulkarni, G. R., Sagan, F., Kok, G. L., Dorsey, J., Nichman, L.,
Rothenberg, D. A., Rösch, M., Kirchgäßner, A. C. R., Ladkin, R., Wex, H., Wilson, T. W., Ladino, L. A., Abbatt, J. P., Stetzer, O.,

555   Lohmann, U., Stratmann, F., and Cziczo, D. J.: The SPectrometer for Ice Nuclei (SPIN): an instrument to investigate ice nucleation,
Atmospheric Measurement Techniques, 9, 2781–2795, https://doi.org/10.5194/amt-9-2781-2016, 2016.

Hiranuma, N., Augustin-Bauditz, S., Bingemer, H., Budke, C., Curtius, J., Danielczok, A., Diehl, K., Dreischmeier, K., Ebert, M., Frank,
F., Hoffmann, N., Kandler, K., Kiselev, A., Koop, T., Leisner, T., Möhler, O., Nillius, B., Peckhaus, A., Rose, D., Weinbruch, S., Wex,
H., Boose, Y., Demott, P. J., Hader, J. D., Hill, T. C. J., Kanji, Z. A., Kulkarni, G. R., Levin, E. J. T., McCluskey, C. S., Murakami, M.,

560   Murray, B. J., Niedermeier, D., Petters, M. D., Saito, A., Schill, G. P., Tajiri, T., Tolbert, M. A., Welti, A., Whale, T. F., Wright, T. P.,
and Yamashita, K.: A comprehensive laboratory study on the immersion freezing behavior of illite NX particles: a comparison of 17
ice nucleation measurement techniques, Atmospheric Chemistry and Physics, 15, 2489–2518, https://doi.org/10.5194/acp-15-2489-2015,
2015.

Hussain, K. and Saunders, C. P. R.: Ice nucleus measurement with a continuous flow chamber, Quarterly Journal of the Royal Meteorological

565 Society, 110, 75–84, https://doi.org/10.1002/qj.49711046307, 1984.

Kanji, Z. A. and Abbatt, J. P.: The university of toronto continuous flow diffusion chamber (UT-CFDC): A simple design for ice nucleation
studies, Aerosol Science and Technology, 43, 730–738, https://doi.org/10.1080/02786820902889861, 2009.

Kanji, Z. A., Ladino, L. A., Wex, H., Boose, Y., Burkert-Kohn, M., Cziczo, D. J., and Krämer, M.: Overview of Ice Nucleating Particles,
Meteorological Monographs, 58, 1.1–1.33, https://doi.org/10.1175/AMSMONOGRAPHS-D-16-0006.1, 2017.

570 Koop, T., Kapilashrami, A., Molina, L. T., and Molina, M. J.: Phase transitions of sea-salt/water mixtures at low temperatures: Implications
for ozone chemistry in the polar marine boundary layer, Journal of Geophysical Research: Atmospheres, 105, 26 393–26 402, https:
//doi.org/10.1029/2000JD900413, 2000a.

Koop, T., Luo, B., Tsias, A., and Peter, T.: Water activity as the determinant for homogeneous ice nucleation in aqueous solutions, Nature,
406, 611–614, https://doi.org/10.1038/35020537, 2000b.

575 Kumar, P., Broekhuizen, K., and Abbatt, J. P.: Organic acids as cloud condensation nuclei: Laboratory studies of highly soluble and insoluble
species, Atmospheric Chemistry and Physics, 3, 509–520, https://doi.org/10.5194/acp-3-509-2003, 2003.

Lacher, L., Lohmann, U., Boose, Y., Zipori, A., Herrmann, E., Bukowiecki, N., Steinbacher, M., and Kanji, Z. A.: The Horizontal Ice
Nucleation Chamber (HINC): INP measurements at conditions relevant for mixed-phase clouds at the High Altitude Research Station
Jungfraujoch, Atmospheric Chemistry and Physics, 17, 15 199–15 224, https://doi.org/10.5194/acp-17-15199-2017, 2017.

580   Lacher, L., DeMott, P. J., Levin, E. J. T., Suski, K. J., Boose, Y., Zipori, A., Herrmann, E., Bukowiecki, N., Steinbacher, M., Gute, E., Abbatt, J. P., Lohmann, U., and Kanji, Z. A.: Background free-tropospheric ice nucleating particle concentrations at mixed-phase cloud conditions, Journal of Geophysical Research: Atmospheres, 123, 10,506–10,525, https://doi.org/10.1029/2018JD028338, 2018.

Lohmann, U. and Feichter, J.: Global indirect aerosol effects: a review, Atmospheric Chemistry and Physics, 5, 715–737, https://doi.org/10.5194/acp-5-715-2005, 2005.

585   Lüönd, F., Stetzer, O., Welti, A., and Lohmann, U.: Experimental study on the ice nucleation ability of size-selected kaolinite particles in the immersion mode, Journal of Geophysical Research, 115, D14 201, https://doi.org/10.1029/2009JD012959, 2010.

Marcolli, C., Gedamke, S., Peter, T., and Zobrist, B.: Efficiency of immersion mode ice nucleation on surrogates of mineral dust, Atmospheric Chemistry and Physics, 7, 5081–5091, https://doi.org/10.5194/acp-7-5081-2007, 2007.

Marcolli, C., Nagare, B., Welti, A., and Lohmann, U.: Ice nucleation efficiency of AgI: Review and new insights, Atmospheric Chemistry

590   and Physics, 16, 8915–8937, https://doi.org/10.5194/acp-16-8915-2016, 2016.

Mignani, C., Creamean, J. M., Zimmermann, L., Alewell, C., and Conen, F.: New type of evidence for secondary ice formation at around -15 °c in mixed-phase clouds, Atmospheric Chemistry and Physics, 19, 877–886, https://doi.org/10.5194/acp-19-877-2019, 2019.

Mülmenstädt, J., Sourdeval, O., Delanoë, J., and Quaas, J.: Frequency of occurrence of rain from liquid-, mixed-, and ice-phase clouds derived from A-Train satellite retrievals, Geophysical Research Letters, 42, 6502–6509, https://doi.org/10.1002/2015GL064604, 2015.

595   Murray, B. J., O'Sullivan, D., Atkinson, J. D., and Webb, M. E.: Ice nucleation by particles immersed in supercooled cloud droplets, Chemical Society Reviews, 41, 6519–6554, https://doi.org/10.1039/C2CS35200A, 2012.

Niemand, M., Möhler, O., Vogel, B., Vogel, H., Hoose, C., Connolly, P., Klein, H., Bingemer, H., Demott, P. J., Skrotzki, J., and Leisner, T.: A particle-surface-area-based parameterization of immersion freezing on desert dust particles, Journal of the Atmospheric Sciences, 69, 3077–3092, https://doi.org/10.1175/JAS-D-11-0249.1, 2012.

600   Petters, M. D. and Wright, T. P.: Revisiting ice nucleation from precipitation samples, Geophysical Research Letters, 42, 8758–8766, https://doi.org/10.1002/2015GL065733, 2015.

Phillips, V. T., Demott, P. J., Andronache, C., Pratt, K. A., Prather, K. A., Subramanian, R., and Twohy, C.: Improvements to an empirical parameterization of heterogeneous ice nucleation and its comparison with observations, Journal of the Atmospheric Sciences, 70, 378–409, https://doi.org/10.1175/JAS-D-12-080.1, 2013.

605   Richardson, M. S., DeMott, P. J., Kreidenweis, S. M., Cziczo, D. J., Dunlea, E. J., Jimenez, J. L., Thomson, D. S., Ashbaugh, L. L., Borys, R. D., Westphal, D. L., Casuccio, G. S., and Lersch, T. L.: Measurements of heterogeneous ice nuclei in the western United States in springtime and their relation to aerosol characteristics, Journal of Geophysical Research Atmospheres, 112, 1–16, https://doi.org/10.1029/2006JD007500, 2007.

Rogers, D. C.: Development of a Continuous Flow Thermal Gradient Diffusion Chamber for Ice Nucleation Studies, Atmospheric Research,

610   22, 149–181, https://doi.org/10.1016/0169-8095(88)90005-1, 1988.

Rogers, R. R. and Vali, G.: Recent developments in meteorological physics, Physics Reports, 48, 65–177, https://doi.org/10.1016/0370-1573(78)90078-9, 1978.

Rogers, R. R. and Yau, M. K.: A short course in cloud physics, Oxford, Pergamon Press. Rosenfeld, 3, illustr edn., 1996.

Saxena, V. K., Burford, J. N., Kassner, J. L., Saxena, V. K., Burford, J. N., and Jr., J. L. K.: Operation of a Thermal Diffusion Chamber for

615   Measurements on Cloud Condensation Nuclei, Journal of the Atmospheric Sciences, 27, 73–80, https://doi.org/10.1175/1520-0469(1970)027<0073:OOATDC>2.0.CO;2, 1970.

Stetzer, O., Baschek, B., Lüönd, F., and Lohmann, U.: The Zurich Ice Nucleation Chamber (ZINC)-A New Instrument to Investigate Atmospheric Ice Formation, Aerosol Science and Technology, 42, 64–74, https://doi.org/10.1080/02786820701787944, 2008.

Sun, Z. and Shine, K. P.: Studies of the radiative properties of ice and mixed-phase clouds, Quarterly Journal of the Royal Meteorological Society, 120, 111–137, http://doi.wiley.com/10.1002/qj.49712051508, 1994.

Sutherland, W.: LXXV. A dynamical theory of diffusion for non-electrolytes and the molecular mass of albumin, The London, Edinburgh, and Dublin Philosophical Magazine and Journal of Science, 9, 781–785, https://doi.org/10.1080/14786440509463331, 1905.

Thielicke, W. and Stamhuis, E. J.: PIVlabTowards User-friendly, Affordable and Accurate Digital Particle Image Velocimetry in MATLAB, Journal of Open Research Software, 2, http://doi.org/10.5334/jors.bl, 2014.

Tomlinson, E. M. and Fukuta, N.: A new horizontal gradient, continuous flow, ice thermal diffusion chamber., Journal of Atmospheric and Oceanic Technology, 2, 448–467, https://doi.org/10.1175/1520-0426(1985)002<0448:ANHGCF>2.0.CO;2, 1985.

Vali, G.: Quantitative Evaluation of Experimental Results an the Heterogeneous Freezing Nucleation of Supercooled Liquids, Journal of the Atmospheric Sciences, 28, 402–409, https://doi.org/10.1175/1520-0469(1971)028<0402:QEOERA>2.0.CO;2, 1971.

Vali, G., DeMott, P. J., Möhler, O., and Whale, T. F.: Technical Note: A proposal for ice nucleation terminology, Atmospheric Chemistry and Physics, 15, 10 263–10 270, https://doi.org/10.5194/acp-15-10263-2015, 2015.

Wex, H., Huang, L., Zhang, W., Hung, H., Traversi, R., Becagli, S., Sheesley, R. J., Moffett, C. E., Barrett, T. E., Bossi, R., Skov, H., Hünerbein, A., Lubitz, J., Löffler, M., Linke, O., Hartmann, M., Herenz, P., and Stratmann, F.: Annual variability of ice-nucleating particle concentrations at different Arctic locations, Atmospheric Chemistry and Physics, 19, 5293–5311, https://doi.org/10.5194/acp-19-5293-2019, 2019.

Zuberi, B., Bertram, A. K., Cassa, C. A., Molina, L. T., and Molina, M. J.: Heterogeneous nucleation of ice in $(NH_4)_2SO_4$-H_2O particles with mineral dust immersions, Geophysical Research Letters, 29, 142–1–142–4, https://doi.org/10.1029/2001GL014289, 2002.